JOURNAL OF GEOPHYSICAL RESEARCH, VOL. 111, B08406, doi:10.1029/2004JB003375, 2006

Click Here for Full Article

Shale diapirism in the Quaternary tectonic evolution of the Northern Apennine, Bologna, Italy

Andrea Borgia,[1] Giovanni Grieco,[2] Fabio Brondi,[1] Marcello Badalì,[1] Olivier Merle,[3] Giorgio Pasquarè,[2] Luca Martelli,[4] and Teresa di Nardo[4]

Received 8 August 2004; revised 10 July 2005; accepted 29 December 2005; published 24 August 2006.

[1] We use morphologic, stratigraphic, and structural data to identify a set of diapirs just southward (uphill) of the northern margin of the Northern Apennine Range. The diapirs consist mainly of Ligurid chaotic shaley units that reach a maximum thickness of over 3 km. We also reconstruct marine sedimentation/abrasion surfaces that record a 1 cm/a differential uplift induced by diapirism. On the basis of this data we use the lubrication approximation of the Navier-Stokes equations and analogue experiments to show that thrusting of the Epiligurid units can be generated by diapirism of the underlying Ligurid units in addition to regional compression. Owing to a gravity component parallel to the strata, the structures formed by diapirism are similar to those generated by compressive tectonics, differing in that thrusting is lubricated by diapiric rise. Using the analogue experiments, we show that deformation begins with folding eventually evolving to thrusting, and we derive an empirical relation to infer the time remaining to the end of deformation. In our area, diapiric deformation is still in the folding regime, but it should eventually evolve to the thrusting regime and terminate in about 10^5 a. We suggest that the whole northeastern slope of the Northern Apennine is controlled by diapiric tectonics. Our interpretation contrasts with the more traditional one, which views regional tectonic compression as the only responsible for the structures observed in the field. Since our model is based on first principles, it could be applied to other areas with similar geology and topography.

Citation: Borgia, A., G. Grieco, F. Brondi, M. Badalì, O. Merle, G. Pasquarè, L. Martelli, and T. di Nardo (2006), Shale diapirism in the Quaternary tectonic evolution of the Northern Apennine, Bologna, Italy, *J. Geophys. Res.*, *111*, B08406, doi:10.1029/2004JB003375.

1. Introduction

[2] Gravity tectonics requires two conditions to leave an imprint in the geological record. The first is a horizontal density gradient, which (by generating aerially heterogeneous vertical pressure gradients) induces flow from high-density to low-density volumes. The second condition depends on rock viscosity. This must be sufficiently small to allow an adequate amount of deformation to be detectable in the geologic record before other processes, such as erosion, may reduce the density gradient, inhibiting further deformation. At the same time, the viscosity must be sufficiently high to avoid fast evolving process such as soil creep or landsliding. Therefore gravity tectonics appears to be characterized by strain rates ranging between 10^{-4} and 10^{-6} a^{-1} and by intervals of about 4 orders of magnitude in space (10^3–10^6 m), time (10^4–10^7 a), and viscosity (10^{17}–10^{20} Pa s).

[3] In this paper we describe the gravitational "skin-tectonics" evolution of a sector of the northeastern slope of the Northern Apennine Range (NAR), close to Bologna City, that falls into the space, time, and viscosity ranges indicated above. We show that gravity-induced flow and diapirism in clayey and shaley formations are so extensively distributed that they substantially overprint and in many cases erase the signature of regional tectonic compression. We base our thesis on a detailed stratigraphic, morphologic, and tectonic study. From these field data we develop a model based on the lubrication approximation of the Navier-Stokes equations and on scaled analogue experiments of the gravitational deformation that characterizes the area. The experimental results show an empirical equation that can describe the evolution of the northeastern slope of the NAR. Since our work is based on fundamental principles, it could be applied to similar geological settings.

2. Regional Geology and Stratigraphy

[4] The NAR is a fold-and-thrust belt of Tertiary age, which developed from an accretionary prism along the

[1]EDRA, Roma, Italy.
[2]Dip. Scienze della Terra "A. Desio," Univ. degli Studi di Milano, Milano, Italy.
[3]Laboratoire Magmas et Volcans, Observatoire de Physique du Globe, Clermont-Ferrand, France.
[4]Servizio Geologico, Sismico e dei Suoli, Regione Emilia-Romagna, Bologna, Italy.

Copyright 2006 by the American Geophysical Union.
0148-0227/06/2004JB003375$09.00

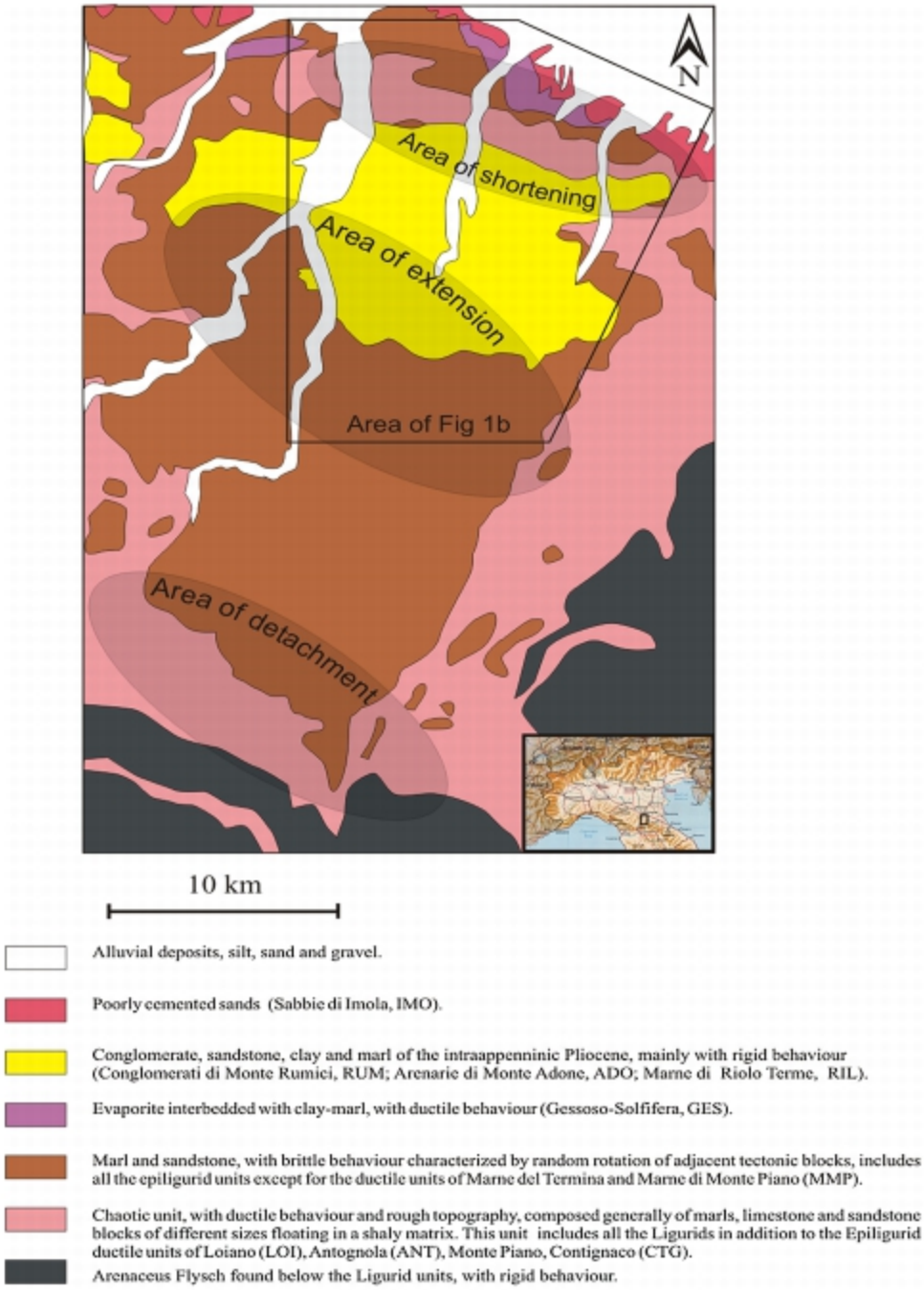

Figure 1a. Geology of the northern slope of the Northern Apennine (NAR) south of Bologna City between the Savena and Idice rivers. Schematic map of ductile and brittle units [after *RER*, 1998]. See inset for location of the study area in the NAR. Note that the ductile chaotic-shaley Ligurid units crop out all around the brittle sandy Epiligurid units, which form diapiric structures.

African and European plates margin [*Treves*, 1984]. During the northeastward displacement of this belt, from Eocene to Lower Pliocene, a set of piggyback basins formed along the northeastern slope of the belt [*Pieri*, 1961; *Lipparini*, 1966; *Ori and Friend*, 1984; *Ricci Lucchi*, 1987; *Bettelli and Panini*, 1987; *Boccaletti et al.*, 1990a, 1990b; *Farabegoli et al.*, 2006; *Panini et al.*, 2002]. The basin's floors are mainly composed of a variably thick succession (ranging from 100 to 1000 m) of chaotic ophiolitic-rich shaley complexes, olistostromes and marls, known as the Ligurid units [*Papani*, 1964; *Abbate et al.*, 1981; *Bettelli and Panini*, 1984, 1987; *Vai and Castellarin*, 1992]. In turn, the Ligurid units were emplaced, at least since Middle Miocene, on the Marnoso Arenacea Formation [*Boccaletti et al.*, 1990b]. Compared to the Marnoso-Arenacea Formation, which tends to show rigid behavior, the Ligurid units have a ductile rheology [*Carena et al.*, 2000].

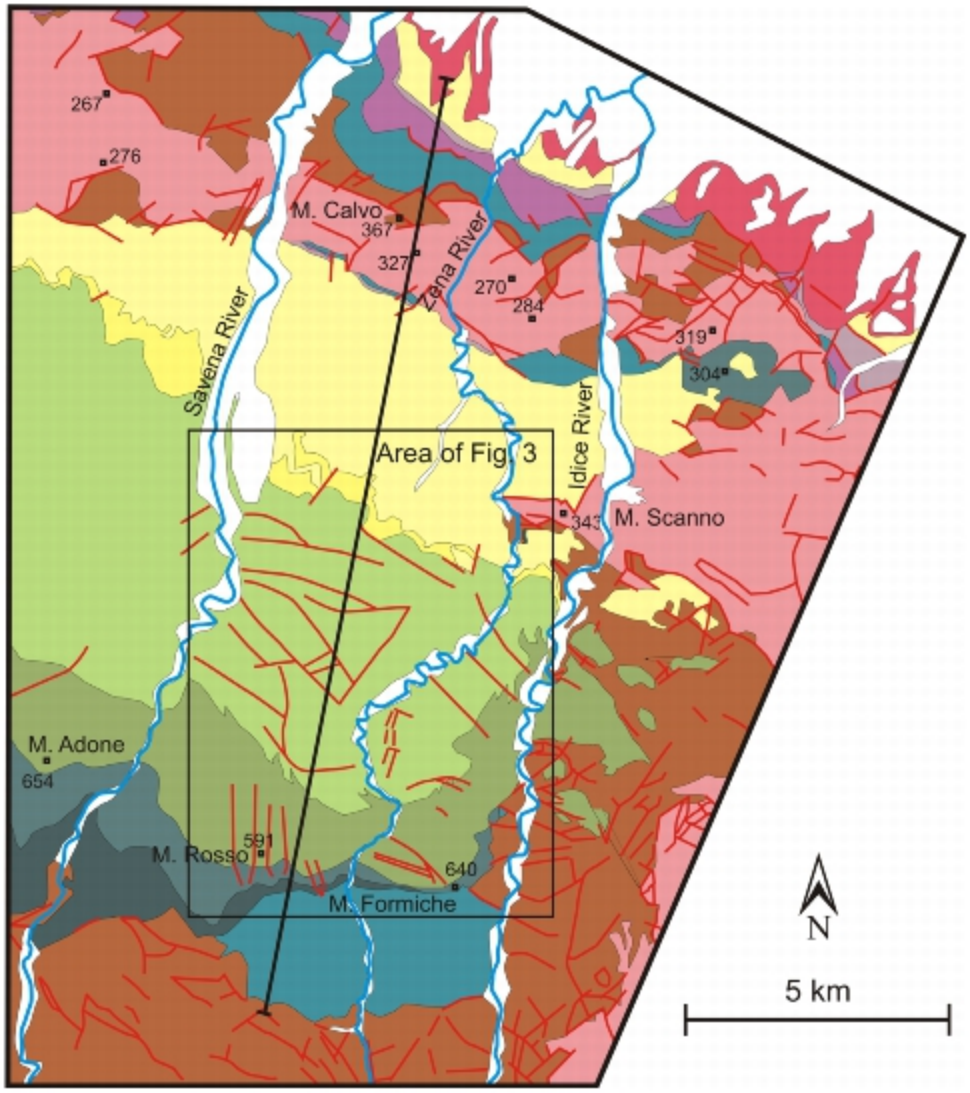

Figure 1b. Detail geology of the study area shown in Figure 1a (after *RER* [2001]; filled boxes with numbers are elevation of summits).

[5] The Epiligurid units (Figures 1a–1d) were deposited above the Ligurids. The lower Epiligurid units are mainly clays and shales and change upward to marls and sandstones. After their deposition the arenaceous units began to deform into brachisynclines separated by narrow and elongated uplifted areas of chaotic shaley units of Ligurids and lower Epiligurids (Figures 1a–1d) [*Borgia et al.*, 1997; *Carena et al.*, 2000].

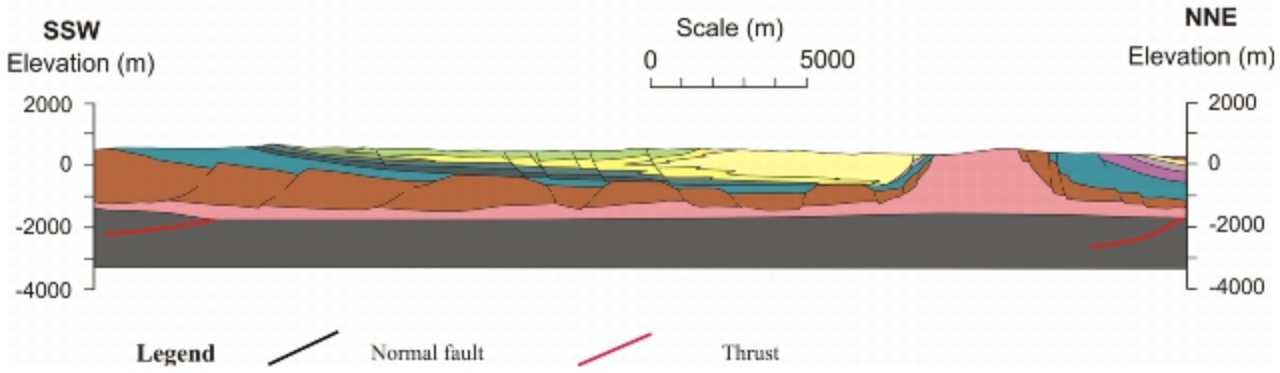

Figure 1c. Geologic cross-section of the study area (modified after *RER* [1998]).

Legend

Trace of geologic section

Thrust fault

Fault (unidentified)

Diapiric thrust

Thrust related fold

Alluvial deposits, silt, sand and gravel.

Poorly cemented sands (Sabbie di Imola, IMO).

Clay and marl with ductile behaviour, involved in plastic deformation, characterized by smooth morfology. (Marne di Riolo Terme, RIL).

Sandstones and shales, with brittle/ductile behaviour Marne di Riolo Terme, RIL_s

Sandstone with brittle behaviour, involved in brittle deformation, associated with rough topography (Arenarie di Monte Adone, ADO), occasionally rich in conglomerates (Arenarie e conglomerati di Monte Mario, ADO_1).

Conglomerate with brittle behaviour, involved in brittle deformation, associated with rough topography and extensive cliffs (Conglomerati di Monte Rumici, RUM_1); fine conglomerate and sand with minor silt (RUM_2).

Clay and marly clay, with ductile behaviour (Argille a Colombacci, COL).

Evaporite interbedded with clay-marl, with ductile behaviour (Gessoso-Solfifera, GES).

Clay with ductile behaviour, involved in plastic deformation, associated with smooth morphology (Marne del Termina, TER).

Marl and sandstone, with brittle behaviour characterized by random rotation of adjacent tectonic blocks, includes all the epiligurid units except for the ductile units of Marne del Termina and Marne di Monte Piano (MMP).

Chaotic unit, with ductile behaviour and rough topography, composed generally of marls, limestone and sandstone blocks of different sizes floating in a shaly matrix. This unit includes all the Ligurids in addition to the Epiligurid ductile units of Loiano (LOI), Antognola (ANT), Monte Piano, Contignaco (CTG).

Arenaceus Flysch found below the Ligurid units, with rigid behaviour.

Figure 1d. Geologic legend common to all figures, unless otherwise indicated.

Figure 2. Photo of planar surfaces occurring between the northern and southern ridges. Looking northeast. Two well-preserved surfaces are clearly visible in the top-center of the photo (indicated by the arrows). These surfaces are located at the eastern end of cross-section D (see Figure 3 and 5). The surface on the right is downthrown by about 50 m relative to the left one.

[6] Since Miocene the compressive orogenic deformations of the foreland (verging NNE) were associated with WNW striking extensional features occurring at the back of the orogenic belt [*Castellarin et al.*, 1986; *Castellarin and Vai*, 1986]. Subsequently, both compressional and extensional tectonics migrated toward NNE, with the extension overprinting the earlier compressional structures. This regional extension, though, has not affected the piggyback basins.

[7] By means of field observations and scaled analytic and analogue modeling, we show that some superficial compressive structures of the piggyback basins appear to have formed by active gravity tectonic as opposed to regional compression; this gravity tectonic has influenced the evolution of the sediments infilling the basins at least since the Oligocene. After emergence from the sea in the Lower-Middle Pleistocene [*Vai and Castellarin*, 1992] gravitational tectonics lead to the formation of brachisynclines bordered by shale diapirs [cf. *Carena et al.*, 2000]. *Bombicci* [1882], *Ogniben* [1953], *Bertocci and Casagli* [1992], and *Cazzoli et al.* [1988] also give evidence of diapiric deformation in the chaotic clayey complexes of the Ligurid units. This gravity tectonic imprints our study area and has formed the Zena syncline and its surrounding prominent shale diapirs, which are focused on in the following sections.

3. Morphology of the Zena-Syncline Area

[8] The youngest sequences of the Epiligurid units are folded in a gentle syncline called the Zena syncline (Figures 1b and 1c). This syncline is cut by the N-S-trending rivers Idice in the east, Zena in the center, and Savena in the west. The syncline is bounded in the north and south by two ridges trending WNW-ESE. The southern ridge is formed by a monocline of conglomeratic and arenaceous rocks that stands above more-erodible clayey rocks. The northern ridge is mainly composed of chaotic clays and reaches more than 300 m above the Po Valley plain.

[9] Generally, the valley morphology is at a younger stage of evolution closer to the two ridges than far away from them. This is justified in the area of the southern ridge because the ridge is made of less-erodible arenaceous lithologies. It is at odd, however, at the northern ridge where rivers cut steep rectilinear cañons in highly erodible shaley rocks and thus they are found in a highly active erosional phase. Similar morphology is repeated at a smaller scale also at the "Scanno" ridge, a ridge located midway of the two major ones along the Zena River. The second-order hydrologic network does not cut the ridges; in fact, to the south of them streams flow southward, opposite to the regional slope.

[10] This younger morphology is characteristic of the ridges only: the clayey units cropping out southward of both ridges have gentle slopes that uniformly degrade toward the Zena River and its tributaries. In addition, south of the ridges, the major rivers (Savena, Zena, and Idice) display a well-developed set of active meanders and fluvial terraces (Figure 1b).

[11] Between the northern and southern ridges the morphology is characterized by a number of planar surfaces (called simply "surfaces" in this paper), which degrade in

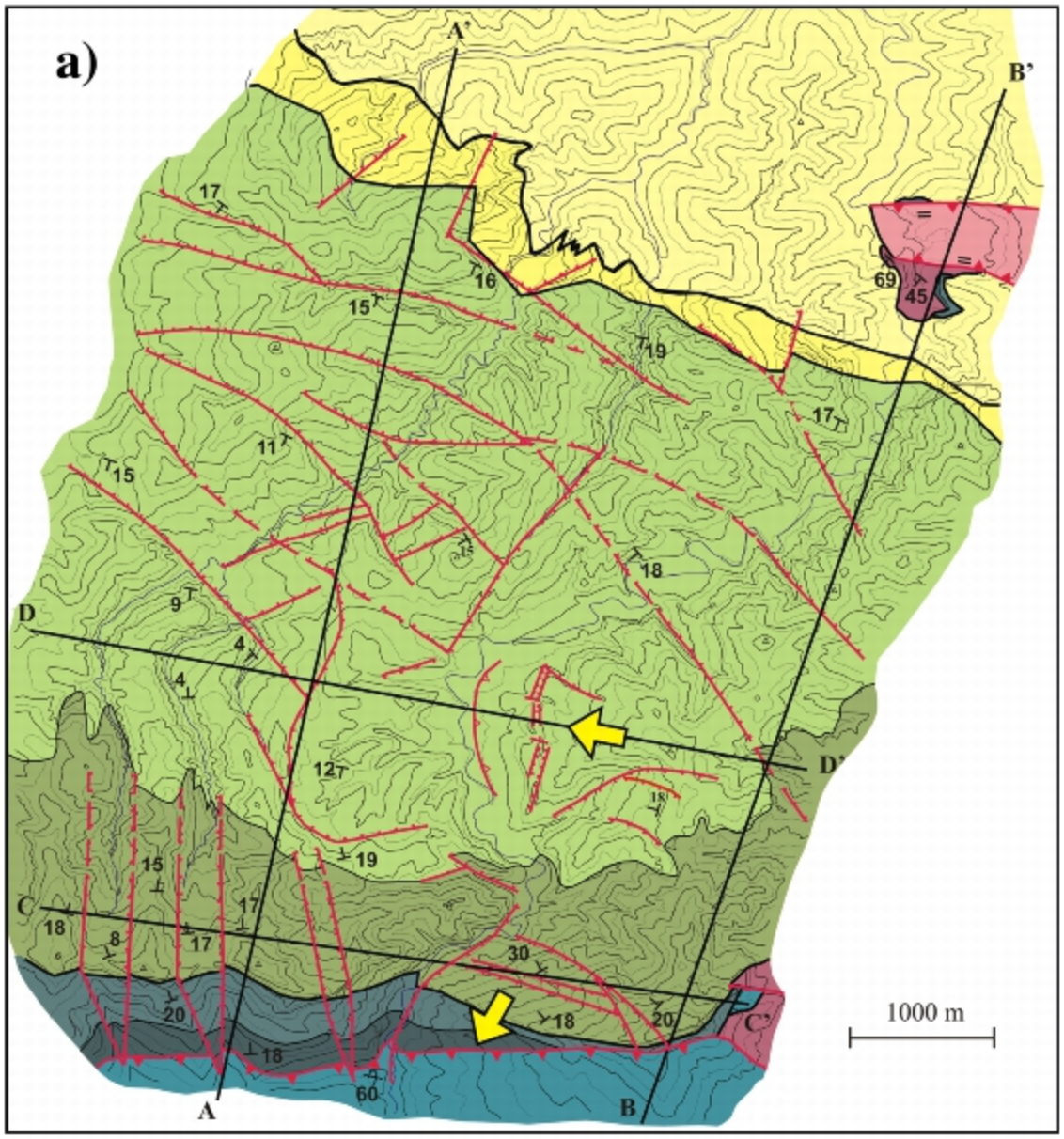

Legend

Diapiric thrust

Normal Fault

Thrust fold

$\perp_{19}$ = Strata attitude with dip, vertical strata

Figure 3

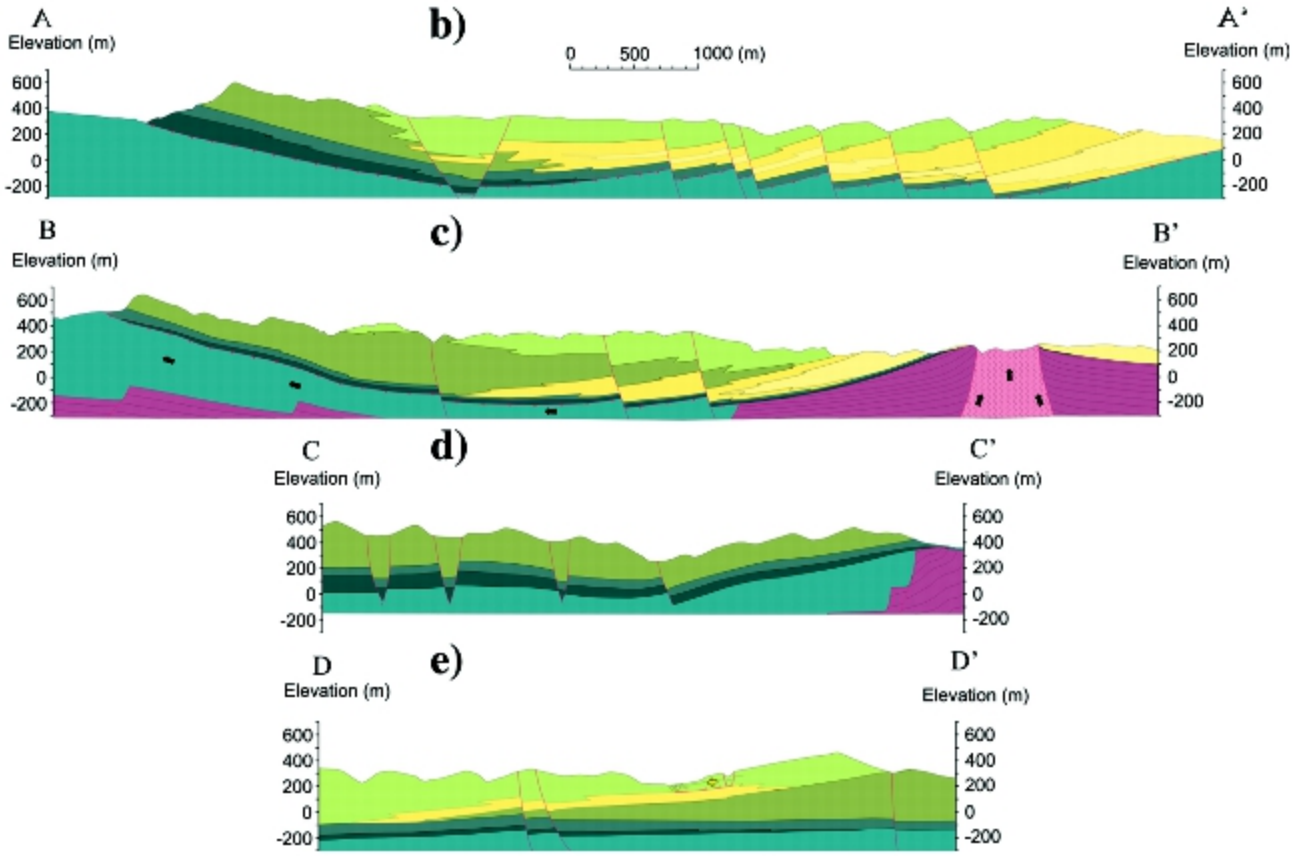

Figure 3. (continued)

elevation away from the two ridges (Figure 2). Such surfaces, which are also found to the north of the northern ridge all the way down to the Po Valley plain [*Parea*, 1987], are very important in understanding the Zena structure and will be described in detail in the following section 6.

4. Structure of the Zena Syncline

[12] The geological maps [*Regione Emilia Romanga* (*RER*), 1997] as well as our detailed geological and structural survey (Figure 3) show that the Plio-Pleistocene terrigenous formations are folded in a gentle syncline with ESE striking major axis and limbs that rise toward the ridges described above. In proximity of the ridges the strata become steeply dipping and occasionally overturned on the middle and northern ridges (Figure 1b, Figures 3b and 3c). The syncline has wavelength of tenths of kilometers and amplitude of about 2 km. The syncline tends to close toward both axial directions forming a brachisyncline (Figure 3a).

[13] Sets of normal faults cut the syncline in adjacent blocks. In general, faults strike parallel or perpendicular to the ridges and are characterized by vertical displacements ranging from 10 to 50 m. Faults parallel to these ridges tend to be listric, downthrowing away from the core of the syncline (Figures 3a and 3b); faults perpendicular to them tend to identify radial horst-and-graben structures (Figures 3a and 3d). The faults are recent and coeval to the folding. In fact, the amplitude of the synclinal folding appears to be falsely enhanced by the listric faulting.

[14] As it has already been noted in the morphology section, a structural anomaly occurs at the middle ridge, the "Scanno" ridge (Figure 3a and 3c). The gentle syncline is pierced by steeply dipping to overturned Epiligurid strata and Ligurid chaotic shales (Figure 4). The contacts between these shales and the surrounding units are tectonic and box-shaped with the shorter side smaller than 500 m in length on outcrop. On the basis of the thickness of the stratigraphic units, we infer a vertical displacement of up to 2 km

Figure 3. Detail geology and structure of the southern part of the study area where the marine sedimentation/abrasion surfaces can still be recognized. After *RER* [1997] and this work, legend in Figures 1a–1d. Traces of the four cross-sections in Figures 3b, 3c, 3d, and 3e are indicated; note the "Scanno" ridge (at the northeast corner) and the unit TER (on the south) shale diapirs. Yellow arrows indicate the displacement direction of major slumps. Figures 3b, 3c, 3d, and 3e show cross-section through the study area (see Figure 1a for location). (b) NNE western cross-section. Note the displacement of units along normal faults above the ductile marl units (TER). (c) NNE eastern cross-section. Note the "Scanno" ridge diapir rising close to the northern end of the section through the Epiligurid units. (d) ESE southern cross-section. Note the horst-and-graben structure along the axis of the southern ridge. (e) ESE northern cross-section. Note the shallow slump structures of the sandstone (ADO) above the clayey units (RIL).

Figure 4. Photo of the shale diapir at "Scanno'' ridge looking east. Observe the chaotic assemblage of heterometric blocks in a shaley matrix and the subvertical pseudolayering.

(Figures 1b and 1c). Such fault shape and throw, along with the fact that the nucleus of the structure is composed of chaotic clays indicate that the "Scanno'' ridge is a diapir, piercing the overlying Epiligurid formations. The topology of the structure of the northern ridge is identical to the one of the "Scanno" ridge. In fact, both diapirs are connected along the eastern margin of the study area (Figures 1a–1d).

[15] Slump structures occur in the southeastern part of the study area. The first of them is a large sakungen occurring just southward (Figure 3a) of the cliff-forming conglomerates (RUM) and sandstones (ADO), which slumps on chaotic silt and clay unit (TER). The second slump structure occurs toward the center of the syncline and appears to be related to basal erosion of sandstone layers (ADO) near the Zena River (Figure 3e). The erosion makes the sandstones laterally unsupported and allows slipping on the underlying siltstones (RIL). This slump ends at the base in a small thrust-related fold that has displaced the Zena River westward.

5. Analysis of Surfaces

[16] Using 1:10 000 geologic maps [*RER*, 1997], 1:10 000 topographic maps, and 1:40 000 aerial photographs, we mapped in detail a 25 km^2 portion of the Zena syncline, where the surfaces identified in the morphologic study are most evident (Figure 5). We also mapped the hillcrests subdividing them in stretches of similar slopes.

[17] Our survey shows that the surfaces have formed due to a number of processes, which include marine and subaerial sedimentation and erosion. We have classified the surfaces based on the process that led to their formation (Figure 5), these are river terraces, erosional surfaces along facies transitions, erosional surfaces along disconformities, erosional surfaces along fault planes, and surfaces generated by marine sedimentation and abrasion. Given their significance for understanding the geodynamic evolution of the area, we briefly describe them below.

[18] 1. Surfaces generated by river sedimentation (terraces) are further subdivided into "present-day," "recent," and "old" river terraces (Figures 1a–1d, and 3). Most of the course of the Zena River occurs in a relatively narrow valley (about 200–400 m wide) in which the meandering river has formed an almost continuous set of "present-day" terraces, where deposition still occurs during major flooding events. "Recent" terraces, on the contrary, have just been sufficiently uplifted above the river to become abandoned. Both types of terraces are practically absent where the Zena River cuts the three ridges (the northern, the "Scanno," and the southern one) and it is in active erosion. "Old" terraces are found only on or close to the "Scanno'' ridge (Figure 5). They have been significantly uplifted by tectonic activity associated with diapirism; their topographic position, relative to the river, topologic relation, relative to the other terraces, and degree of erosion suggest that they were formed during the Olocene. All these abovementioned facts indicate that the three ridges have been and still are actively uplifting.

[19] 2. Differential erosion along the facies transition (Figures 1a–1d, and 3) between the sandstones (ADO) to the south and the clays (RIL) to the north has generated a cliff a few tens of meters high. This cliff is fairly continuous and it occurs throughout the study area from ESE to WNW.

[20] 3. Differential erosion along the disconformity (Figures 1a–1d, and 3) existing between the conglomerates (RUM) and sandstones (ADO) with the dismembered clays (TER), in the south of the study area, has generated a most prominent cliff: the clays to the south have been more rapidly eroded than the conglomerates and sandstones to the north. This cliff is up to a few hundred meters high and has a regional extent with ESE strike (Figure 6).

[21] 4. Surfaces, which are erosional remnants of fault planes, are common in our area, particularly where the faults cut conglomerates and sandstones. Frequently, the stratigraphy on either side of the faults allows the reconstruction of fault's displacement. These surfaces are less evident in silty and clayey lithologies. The identification of this kind of surfaces that should not be confused with the surfaces related to point 2 above, allows the detailed reconstruction of the set of normal faults that dissect the Zena Syncline.

[22] 5. Surfaces generated by marine sedimentation now form broad, uplifted, tilted, and faulted areas. In the Zena Valley we have recognized a large number of these surfaces (Figure 5). They are composed of poorly consolidated terrigenous sediments and they are parallel to the bedding. These surfaces are not associated with any kind of conti-

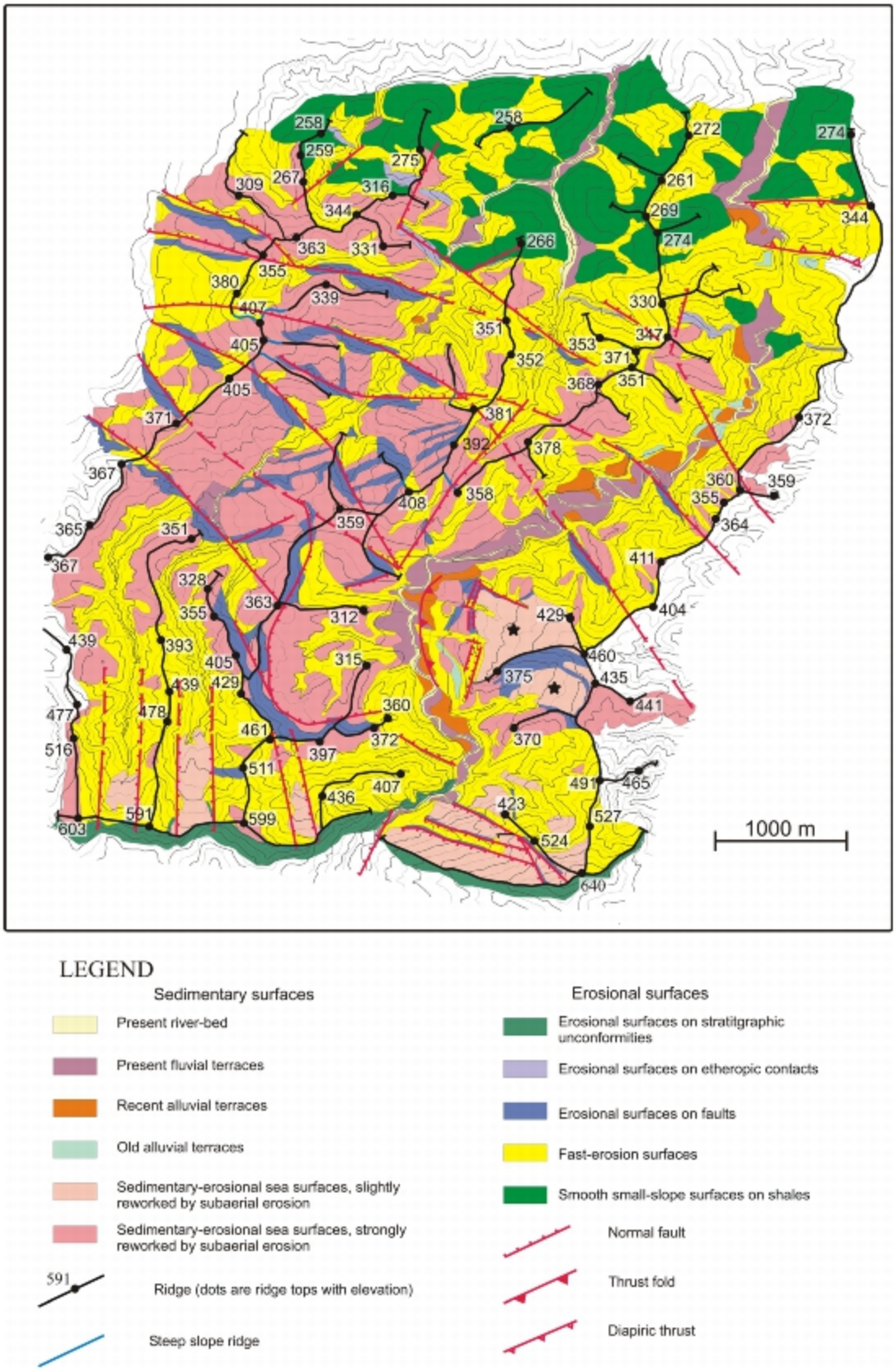

Figure 5. Map of sedimentary, tectonic and erosional surfaces present in the study area. Black stars show surfaces of Figure 2. Major ridges and faults are also indicated.

Figure 6. Photograph of the southern ridge. The sandstone and conglomerate (RUM and ADO) form the cliffs, while the clay and marls (TER) form the smooth morphology on the center-left of the photo.

nental deposit, with the exception of restitic soil. The stratigraphic and structural framework indicates that these surfaces are portions of an originally continuous surface, which formed at the end of marine sedimentation. This surface was subsequently uplifted above sea level and then deformed in a synform and dismembered by tectonic activity (Figure 2). In many cases, subaerial erosion has modeled the original planar surface into mild hills cut by clefts of creeks that are still actively eroding.

[23] 6. Marine sedimentation surfaces are totally absent in the northern part of the area northward of the sandstone-clay facies transition, where the clayey lithology has not allowed their preservation from erosion. In this part of the area (Figure 5) the hills slope mildly toward the creeks. However, the ridges maintain almost constant elevation for their whole extent (Figure 5). Only toward the northern and the "Scanno" ridges they tend again to rise to higher elevations being uplifted by the rising diapirs. We interpret these ridges at constant elevation as the remains of a marine abrasion plane formed in front of a cliff, (see point 2 above), generated by differential erosion of the clays (RIL) with respect to the sandstones (ADO).

[24] Figure 7 is a reconstruction of the original surface formed by the final sedimentation and marine abrasion (see points 5 and 6, respectively, above), as it would be today after removal of subaerial erosion. This reconstruction shows the folding and faulting of this surface (and of the underlying rock units) due to gravity tectonic. The surface must have been deformed after the emergence from the sea, which occurred later than the Middle Pleistocene [*Di Dio et al.*, 1997a, 1997b], because it must have been horizontal at the end of its formation, just before the emergence.

[25] Our reconstruction of the marine surface allows us the identification of two units, in addition to the Ligurid, which, due to their ductile behavior, induced gravitational tectonics. The first of them are the TER chaotic clayey marls. We deduce that the conglomerates (RUM) and sandstones (ADO) found above sank into the TER giving rise to the southern flank of the Zena brachisyncline. Similar structures are found farther west on the NAR [*Borgia et al.*, 1997; *Carena et al.*, 2000]. The second (uppermost) ductile layers in the stratigraphy are the RIL clays and marls. They are responsible for the second slump described previously in section 5 (see Figures 3a and 3e).

[26] In the following analysis, we will attempt to model the gravity deformation related to the Ligurid units, which form the lowermost ductile layer. This deformation influences all the overlaying rock units, including those that form the Zena syncline, as well as of the slumps described above. The syncline and the slumps, though, are further deformed by a gravity deformation that is rooted at higher stratigrafic levels than the ligurids.

6. Analysis of Gravity Tectonics

[27] To analyze the effect of diapirism on the tectonics observed in our study area, specifically Figure 1a, we made a simple model composed of a box with a rigid basement (Figure 8), which corresponds to the arenaceous Tuscan and Romagna units (that are found below the Ligurids), overlaid by a ductile layer, which represents the chaotic clayey Ligurid units. Effectively, as described above and observed in other areas of the Apennine [*Carena et al.*, 2000], the Ligurid units display a clear ductile behavior since they form conspicuous diapirs; their ductile behavior is due to the large clay fraction, perhaps combined with overpressure and sufficiently low strain rates. In turn, the ductile layer is overlaid by a brittle layer, which represents the arenaceous Epiligurid units.

[28] As observed in our area the layers have a dip of an angle α and, whereas the upper brittle layer tends to maintain a constant thickness, the ductile layer pinches out northward. The lateral boundaries of the experimental box are rigid and fixed, while the upper boundary of

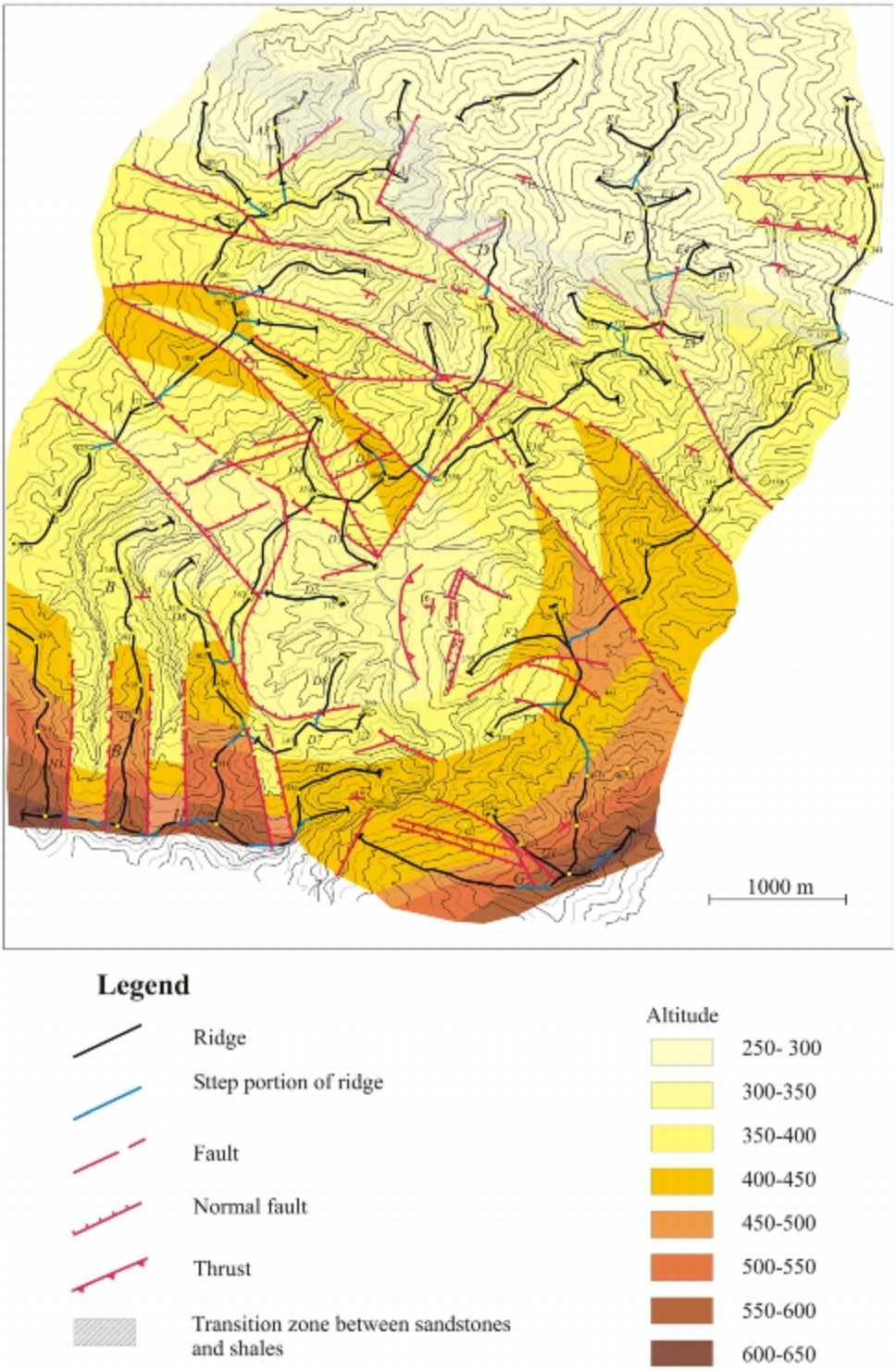

Figure 7. Reconstruction of the marine sedimentation/abrasion surface as it is today after removal of subaerial erosion. Note the horst-and-graben structures and brachisyncline in the south, and the set of normal faults that deform the surface. This reconstruction is obtained using the morphologic and topographic data on surfaces and ridges (cf. Figure 5), and the structural data on strata attitude and faults (cf. Figure 3). The surface follows the topography and strata attitude of the least eroded parts of the youngest units (ADO), being cut and displaced by normal faults.

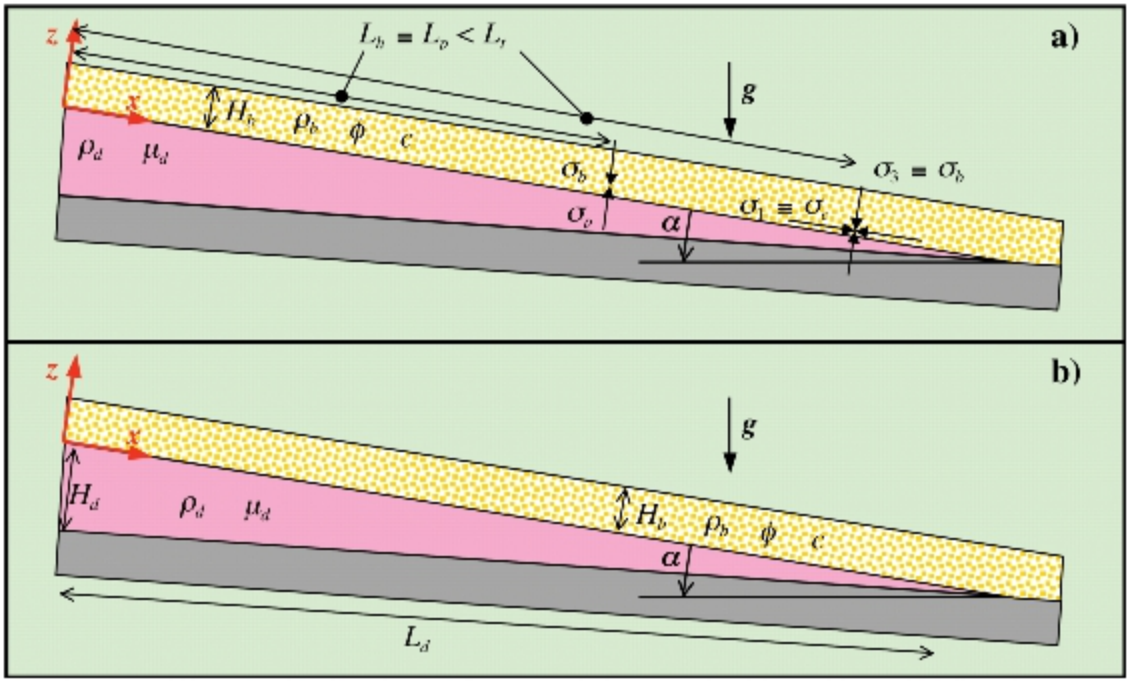

Figure 8. Sketch of the analytic and analogue modeling. In orange, pink, and gray are the brittle layer, the ductile layer and the rigid basement, respectively. See text for explanation.

the model is unconstrained and at constant atmospheric pressure.

6.1. Stationary Case

[29] First, we analyze the stationary case (Figure 8a). In this case, as there must be hydrostatic pressure in the ductile layer, the downhill section of the brittle layer is being pushed upward by the hydrostatic pressure (σ_p) given by

$$\sigma_p = L_p \rho_d g \sin\alpha, \tag{1}$$

where L_p, ρ_d, and g are the distance from the origin along the x axis in the ductile layer, the density of the ductile layer, and the gravity acceleration, respectively. It should be noted that σ_p increases with L_p. In the downhill section of the model, the pressure (σ_b) opposing the hydrostatic uplift is the weight of the brittle layer, given by

$$\sigma_b = \Delta H_b \rho_b g \cos\alpha, \tag{2}$$

where ΔH_b and ρ_b are the difference in thickness between the lower and upper sections of the brittle layer and its density, respectively. It is noteworthy that this pressure is zero when the brittle layer has constant thickness (that is $\Delta H_b = 0$). Once the hydrostatic pressure overcomes the load of the brittle layer, the ductile layer will uplift the brittle layer and form a diapir. The distance L_h at which this occurs is obtained by equating the pressures of equations (1) and (2) and by solving for L_p

$$L_h \equiv L_p = \left(\frac{\rho_b}{\rho_d}\right)\frac{\Delta H_b}{\tan\alpha}, \tag{3}$$

that is, this length is zero when the brittle layer has constant thickness. The component of the weight of the brittle layer in the x-direction (σ_c) is balanced by the elastic forces within the brittle layer itself and is given by

$$\sigma_c = \frac{1}{H_b}\int_0^{L_c} \rho_b g \sin\alpha H_b \partial x = \rho_b g \sin\alpha L_c, \tag{4}$$

where L_c is the distance in the x-direction where σ_c is estimated. The distance at which σ_c becomes larger than the compressive resistance of the brittle layer (σ_t), giving rise to a thrust, may be estimated using the Coulomb fracture criteria,

$$\sigma_t \equiv \sigma_1 = \frac{1+\sin\phi}{1-\sin\phi}\sigma_3 + \frac{2\cos\phi}{1-\sin\phi}c, \tag{5}$$

where σ_1 is the maximum stress, σ_3 is the minimum stress, and ϕ and c are the angle of internal friction and the cohesion of the brittle layer, respectively. Observing that $\sigma_1 = \sigma_c$ (equation (4)) and $\sigma_3 = \sigma_b$ (equation (2)) and solving for the distance (L_t) at which the thrust forms, we find

$$L_t = \left(\frac{1+\sin\phi}{1-\sin\phi}\right)\frac{H_b}{\tan\alpha} + \frac{2\cos\phi}{\rho_b g \sin\alpha(1-\sin\phi)}c, \tag{6}$$

which is always greater than zero. Comparing equations (3) and (6) for any reasonable value of the angle of internal friction for a brittle material (that is $\phi \geq 10°$), even for rocks with no cohesion, and with $\Delta H_b = H_b$ we deduce

$$\frac{\rho_b}{\rho_d} < 1.4 < \frac{1+\sin\phi}{1-\sin\phi} \rightarrow L_h L_t. \tag{7}$$

Therefore the length of brittle layer necessary for diapirism (L_h) is always smaller than the length needed for gravitational thrusting (L_t). Therefore in the case of the NAR, diapirism should prevail over gravitational thrusting, and may significantly overprint the signature of regional tectonics. This component has never been taken into adequate consideration in evaluating the tectonic evolution of the Range, which is generally assumed to result from regional tectonics only [cf. *Picotti et al.*, 1997].

[30] Clearly, once the diapirism in the ductile layer uplifts the brittle layer, the x-component of the pressure in the brittle layer (σ_c) is no longer compensated by the elastic forces within it. As a consequence, the brittle layer will begin to slide downward stretching the rising diapir. Although we have not investigated in detail the transitions from simple diapirism to diapiric thrusting, from the experimental work presented below (see Figures 10, 11, and 12) we deduce that the brittle layer goes through an early stage of folding, eventually forming a thrust. We call these structures diapiric fold and diapiric thrust to stress the role of diapirism in their formation. In fact, the fold and thrust are actually initiated and lubricated by diapirism and are not the direct result of "regional tectonic shortening" within the experimental box, although "regional tectonics" remains essential in generating the tilting of our box.

[31] It is also important to observe that in a thrust, one can usually identify a relatively thin layer (surface) across which most of the deformation occurs. In a diapiric thrust, on the contrary, the deformation involves the whole volume of the diapir and not just the contact between the encasing units.

[32] As the diapiric thrust develops, extensional stresses will build up in the uphill section of the brittle layer. These stresses are balanced by elastic stresses until they overcome the Coulomb extensional fracture limit. This limit is essentially established by the strength of the brittle layer. The maximum value of the extensional stress (σ_e), equivalent to the minimum principal stress, that the brittle layer is able to balance before rupture, is estimated solving equation (5) for σ_3:

$$\sigma_e \equiv \sigma_3 = \left(\frac{1-\sin\phi}{1+\sin\phi}\right)\sigma_1 - \left(\frac{2\cos\phi}{1+\sin\phi}\right)c \leq 0. \tag{8}$$

In this equation, $\sigma_1 = \sigma_b$ is given by equation (2). The value of the cohesion may be approximated by the height of the subvertical cliffs (H_s) occurring in the rocks that form the brittle layer [*Philipponat and Hubert*, 1997; *Merle et al.*, 2001]

$$c \approx \frac{1}{4}\rho_b g H_s \sqrt{\frac{1-\sin\phi}{1+\sin\phi}}. \tag{9}$$

Combining equations (8), (2), and (9), we obtain

$$\sigma_e = \left(\rho_b g \cos\alpha \frac{1-\sin\phi}{1+\sin\phi}\right)H_b - \frac{1}{2}\left(\frac{\rho_b g \cos\phi}{1+\sin\phi}\sqrt{\frac{1-\sin\phi}{1+\sin\phi}}\right)H_s. \tag{10}$$

In the study area, we may assume for the brittle layer $H_b \geq 1000$ m, $\rho_b = 2500$ kg m^{-3}, $\phi = 30°$, and $\alpha = 3°$. Since, for the highest scarps $H_s \leq 100$ m, using $g = 9.8$ m s^{-2}, we calculate

$$\sigma_e \geq 8.16 * 10^6 - 4.08 * 10^5 \geq 7.75 * 10^6 \quad \text{(Pa)}, \tag{11}$$

or, observing that the second (cohesion) term is negligible with respect to the first,

$$\sigma_e \geq \frac{1}{3}\sigma_b. \tag{12}$$

To sum up, we conclude that a relatively small reduction in σ_3, without ever becoming negative, is sufficient to initiate extensional tectonics in the uphill part of the brittle layer. Therefore following the hypothesis used in our model, the necessary and sufficient condition for triggering of compressive and extensional diapiric tectonics is that given by equation (3).

6.2. Dynamic Case

[33] The parameters we adopt for the analysis of the deformation of the ductile layer in the dynamic case are indicated in Figure 8b. We use the lubrication approximation of the Navier-Stokes equations, which includes the pressure and gravity stresses as deforming terms, may be written for the ductile layer as [*Bird et al.*, 1960]:

$$\begin{cases} \dfrac{\partial v_x}{\partial x} + \dfrac{\partial v_z}{\partial z} = 0 & \text{conservation of mass} \quad (13a) \\ -\dfrac{\partial p}{\partial x} + \mu_d \dfrac{\partial^2 v_x}{\partial z^2} + \rho_d g \sin\alpha = 0 & \text{conservation of x-momentum} \quad (13b) \\ \dfrac{\partial p}{\partial z} - \rho_d g \cos\alpha = 0 & \text{conservation of z-momentum} \quad (13c) \end{cases}$$

To derive this approximation, we use the standard viscous-scaling analysis with the following dimensionless variables, which are defined using educated guesses of the maximum values that the dimensional variables can reach in our model (see Figure 8b),

$$x^* = \frac{x}{L_d}; \quad z^* = \frac{z}{H_d}; \quad h^* = \frac{h}{H_d}; \quad t^* = \frac{t}{T}; v_x^* = \frac{v_x}{V_x}; \quad v_z^* = \frac{v_z}{V_z}; \quad p^* = \frac{p}{P_d}. \tag{14}$$

Our approximation implies the following conditions:

$$\frac{H_d}{L_d} = \tan\alpha \ll 1 \tag{15a}$$

$$\frac{H_d}{L_d \tan\alpha} = O(1) \tag{15b}$$

That is, for the gravity term to be significant in both x and z, H_d/L_d should be of the same order of magnitude as $\tan\alpha$,

Table 1. Dimensionless Numbers Used in the Scaling Analysis

Meaning of Number	Dimensionless Number	Equation Number
Ratio between regional slope and angle of internal friction.	$\Pi_1 = \frac{\alpha}{\phi} < 1$	(21a)
Ratio between brittle and ductile densities.	$\Pi_2 = \frac{\rho_b}{\rho_d}$	(21b)
Ratio between system geometry and regional slope.	$\Pi_3 = \frac{H_d}{L_d \tan\alpha} \approx 1$	(21c)
Ratio between system geometry and densities, buoyancy force.	$\Pi_4 = \frac{H_b \rho_b}{H_d \rho_d} \approx 1$	(21d)
Ratio between cohesion and internal friction forces.	$\Pi_5 = \frac{2c\cos\phi}{(1-\sin\phi) H_b \rho_b g \cos\alpha}$	(21e)
Ratio between inertia and viscous forces, Reinolds number.	$\Pi_6 = \frac{\rho_d H_d V_x}{\mu_d} < 1$	(21f)
Ratio between pressure and viscous forces.	$\Pi_7 = \frac{P_d H_d^2}{\mu_d V_x L_d} = 1$	(21g)
Ratio between gravity and viscous forces.	$\Pi_8 = \frac{H_d^2 \rho_d g \sin\alpha}{\mu_d V_x} = 1$	(21h)
Ratio from mass balance.	$\Pi_9 = \frac{L_d V_z}{H_d V_x} = \frac{V_z}{\tan\alpha V_x} = 1$	(21i)
Ratio between process and system evolution times.	$\Pi_{10} = \frac{3\mu_d L_d^2}{H_d^3 T \rho_d g \cos\alpha} \approx 1$	(21j)

and both much smaller than 1. In other words, equation (13) is applicable for a thin viscous layer on a small slope.

[34] The boundary conditions for equation (13a) are

$$v_z|_{z=0} = 0 \tag{16a}$$

$$v_z|_{z=h} = \int_{v_z|_{z=0}}^{v_z|_{z=h}} \partial v_z = \frac{dh}{dt} \tag{16b}$$

The first of these boundary conditions implies mass continuity across the lower boundary, between the rigid basement and the ductile layer; the second condition is characteristic of a free boundary and implies that the vertical velocity of the top of the ductile layer is equal to the time change in ductile layer thickness $h(x, t)$.

[35] A reasonable condition for both lower and upper boundaries in equation (13b) is no slip. For the lower boundary this implies

$$v_x|_{z=0} = 0 \tag{16c}$$

For the upper boundary we must impose a constant stress condition. In fact, because of the diapiric rise in the lower section of our model (see conclusions derived from equation (7)), the x-component of weight in the brittle layer is not balanced by the elastic forces within it and must be balanced by the viscous forces of the deforming ductile layer. That is,

$$\left.\frac{\partial v_x}{\partial z}\right|_{z=h} = -\frac{\rho_b g \sin\alpha H_b}{\mu_d}. \tag{16d}$$

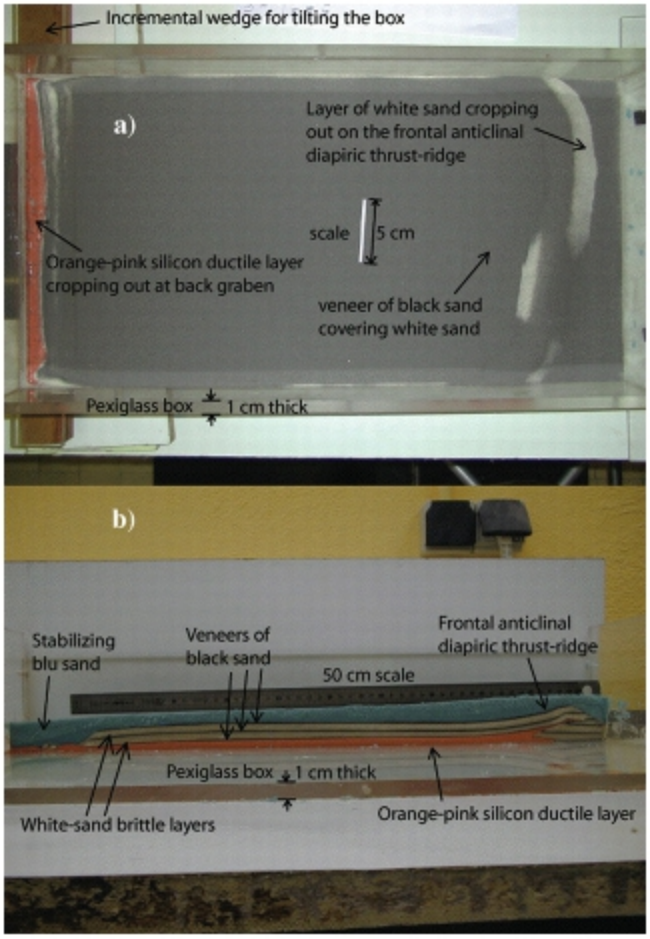

Figure 9. Photos of a characteristic analogue experiment (experiment 5, Table 3). (a) Top view. (b) Side view of the same experiment shown in Figure 9a at the end of deformation (after tilting the model back to horizontal and slicing the model). The blue sand is added at the end of each experiment to prevent further deformation.

Finally, the boundary condition for equation (13c) is

$$p|_{z=h} = P_b(x,t) = \rho_b g \cos\alpha H_b + P_0. \tag{16e}$$

The condition for the pressure $P_b(x, t)$ given by equation (16e) is a function of the thickness and density of the brittle layer and of the pressure (P_0) at the upper surface. This condition satisfies the boundary condition for the pressure also in equation (13b) because equations (13b) and (13c) are coupled through pressure in addition to gravity.

[36] Integrating equation (13) with the boundary conditions given by equation (16) and combining the results, we find

$$\frac{\partial h}{\partial t} = \frac{\rho_d g \cos\alpha}{3\mu_d}\frac{\partial}{\partial x}\left\{h^3\frac{\partial}{\partial x}\left[-x\tan\alpha + h. - \frac{3}{2}H_b\tan\alpha\left(\frac{\rho_b}{\rho_d}\right)\int\left(\frac{1}{h}\right)\partial x\right]\right\}. \tag{17}$$

Using the scaled dimensionless variables in equation (14) in addition to the conditions imposed by equation (15), we may write equation (17) as

$$\frac{3\mu_d L_d^2}{\rho_d g\cos\alpha T H_d^3}\frac{\partial h^*}{\partial t^*} = \frac{\partial}{\partial x^*}\left\{h^{*3}\frac{\partial}{\partial x^*}\left[-x^* + h^*. - \frac{3}{2}\left(\frac{H_b\rho_b}{H_d\rho_d}\right)\int\frac{1}{h^*}\partial x^*\right]\right\}. \tag{18}$$

If our scaling is correct, all terms in this equation, except the first fraction and the fraction before the integral, for which we still have imposed no constraints, tend to vary between 0 and 1; that is, they are of order unit. Therefore the differentials on either side of the equal sign are both significant only if the first fraction is of order unit as well. Thus since the time T needed to complete the process remains unconstrained, we may obtain an order-of-magnitude estimate of it by setting:

$$\frac{3\mu_d L_d^2}{\rho_d g\cos\alpha T H_d^3} = O(1) \Rightarrow T = \frac{3\mu_d L_d^2}{\rho_d g\cos\alpha H_d^3}. \tag{19a}$$

The same argument can be applied to the fraction before the integral sign, obtaining

$$\frac{H_b\rho_b}{H_d\rho_d} = O(1). \tag{19b}$$

That is, in the order of magnitude, if the brittle layer is much thinner than the ductile layer, the deformation dynamics of the second is not influenced by the first. Conversely, if the brittle layer is much thicker than the ductile layer, the ductile layer behaves as decollement, as opposed to a diapir, relative to the brittle layer.

[37] These approximations reduce equation (18) to

$$\frac{\partial h^*}{\partial t^*} = \frac{\partial}{\partial x^*}\left\{h^{*3}\frac{\partial}{\partial x^*}\left[-x^* + h^* - \frac{3}{2}\left(\frac{H_b\rho_b}{H_d\rho_d}\right)\int\frac{1}{h^*}\partial x^*\right]\right\}. \tag{20}$$

6.3. Scaled Experiments

[38] We find approximate solutions to equation (20) using analogue experiments. In order to scale the experiments using the Buckingham-Π theorem [*Bird et al.*, 1960], we

Table 2. Geometry of Experimental Box and Physical Properties of Material Used

Parameter	Units	Value
Experimental box		
L	m	0.585
W	m	0.295
Sand–brittle layer		
ρ_b	kg m^{-3}	1400
c	Pa	10
ϕ	Deg	30
Silicon–viscous layer		
ρ_d	kg m^{-3}	1350
μ_d	Pa s	10^4
Gravity acceleration, g	m s^{-2}	9.8

Table 3a. Experimental Results for Experiments 1a, 1b, 2a, 2b, and 3a

Parameter	Units	Exp. 1a	Exp. 1b	Exp. 2a	Exp. 2b	Exp. 3a
A lower slope of silicon	deg	3	6	3	6	0.1
			Brittle Layer			
H_b	m	0.0110	0.0110	0.0075	0.0075	0.0070
ρ_b	kg m^{-3}	1.40E+03	1,40E+03	1.40E+03	1.40E+03	1.40E+03
c	Pa	1.00E+01	1.00E+01	1.00E+01	1.00E+01	1.00E+01
φ	deg	30	30	30	30	30
			Ductile Layer			
L_d	m	0.2950	0.2950	0.2950	0.2950	0.2300
H_d	m	0.0100	0.0100	0.0093	0.0093	0.0100
ρ_d	kg m^{-3}	1.35E+03	1.35E+03	1.35E+03	1.35E+03	1.35E+03
μ_d	Pa s	1.00E+04	1.00E+04	1.00E+04	1.00E+04	1.00E+04
			Result			
Deformation	bolean	FALSE	TRUE	FALSE	TRUE	FALSE
Structure Type		No deformation	One frontal diapiric thrust. Back diapiric extension, 1 horst.	Deformation is limited to 2 mm downdrop of sand at the uphill edge of the sand in contact with the box.	Diapiric thrust. Applied erosion on one side of thrust. Back diapiric extension, 2 horsts.	No deformation.
			Time			
Time to start of deformation	s	-	7.9200E+03	-	4.8000E+03	-
Time to end of deformation	s	-	1.2132E+05	-	1.8330E+05	-
Time to end of experiment	s	1.4778E+05	3.7152E+05	5.7900E+04	2.1600E+06	4.8000E+02
			Structure			
L_t	m	0	0.0435	0	0.037	0
ΔH_t	m	0	0.0104	0	0.011	0
L_g	m	0	0.0127	0.0069	0.008	0
ΔH_g	m	0	0.0032	0.0020	0.004	0
L_h	m	0	0.0056	0	0.012	0
			Velocities			
V_x	m s^{-1}	0.00E+00	2.43E-06	0.00E+00	1.61E-06	0.00E+00
V_z	m s^{-1}	0.00E+00	8.24E-08	0.00E+00	5.07E-08	0.00E+00
V_x thrusting	m s^{-1}	0.00E+00	3.58E-07	0.00E+00	2.02E-07	0.00E+00
			Π *Numbers*			
Π_1 regional slope/internal friction		1.00E-01	2.00E-01	1.00E-01	2.00E-01	3.33E-03
Π_2 density ratio		1.04E+00	1.04E+00	1.04E+00	1.04E+00	1.04E+00
Π_3 ductile thickness/length ratio		6.47E-01	3.23E-01	6.02E-01	3.00E-01	2.49E+01
Π_4 brittle/ductile thickness ratio		1.14E+00	1.14E+00	8.36E-01	8.36E-01	7.26E-01
Π_5 cohesive/lithostatic ratio		2.30E-01	2.31E-01	3.37E-01	3.39E-01	3.61E-01
Π_6 inertial/viscous ratio		0.00E+00	3.28E-09	0.00E+00	2.02E+00	0.00E+00
Π_7 pressure/viscous ratio		-	1.83E+00	-	2.23E+00	-
Π_8 gravity/viscous ratio		-	5.69E+00	-	7.43E+00	-
Π_9 velocities ratio		-	1.00E+00	-	1.00E+00	-
Π_{10} process rate ratio		1.34E+00	1.64E+00	4.24E+00	1.35E+00	2.50E+02

Table 3b. Experimental Results for Experiments 3b, 3c Right, 3c Center, 4 Right, and 4 Center

Parameter	Units	Exp. 3b	Exp. 3c Right	Exp. 3c Center	Exp. 4 Right	Exp. 4 Center
A lower slope of silicon	deg	3	6	6	6	6
			Brittle Layer			
H_b	m	0.0070	0.0070	0.0070	0.0095	0.0085
ρ_b	kg m^{-3}	1.40E+03	1,40E+03	1.40E+03	1.40E+03	1.40E+03
c	Pa	1.00E+01	1.00E+01	1.00E+01	1.00E+01	1.00E+01
φ	deg	30	30	30	30	30
			Ductile Layer			
L_d	m	0.2300	0.2300	0.2300	0.5350	0.5350
H_d	m	0.0100	0.0100	0.0078	0.0140	0.0140
ρ_d	kg m^{-3}	1.35E+03	1.35E+03	1.35E+03	1.35E+03	1.35E+03
μ_d	Pa s	1.00E+04	1.00E+04	1.00E+04	1.00E+04	1.00E+04
			Result			
Deformation	bolean	FALSE	TRUE	TRUE	TRUE	TRUE
Structure Type		Deformation is limited to 3.8 mm downdrop of sand at the uphill edge of the sand in contact with the box.	Diapiric thrust in front and diapir at back. With erosion thrust moves only a small amount.	Small diapiric thrust and backthrust in front and diapir at back. Slower deformation.	Three diapiric thrusts at the front. Diapiric extension on back with two plates.	Three diapiric folded thrusts at the front. Diapiric extension on back with one plate.
			Time			
Time to start of deformation	s	-	0.0000E+00	4.8000E+04	2.7000E+03	2.7000E+03
Time to end of deformation	s	-	1.7688E+05	2.5092E+05	1.3560E+05	1.3560E+05
Time to end of experiment	s	1.3800E+04	3.3612E+05	3.3612E+05	1.6650E+05	1.6650E+05
			Structure			
L_t	m	0	0.0194	0.0068	0.102	0.099
ΔH_t	m	0	0.009	0.0045	0.022	0.022
L_g	m	0.0132	0.018	0.0115	0.06	0
ΔH_g	m	0.003810512	0	0.0000	0.095	0
L_b	m	0	0	0	0.032	0
			Velocities			
V_x	m s^{-1}	0.00E+00	1.30E-06	9.17E-07	3.95E-06	3.95E-06
V_z	m s^{-1}	0.00E+00	5.65E-08	3.11E-08	1.03E-07	1.03E-07
V_x thrusting	m s^{-1}	0.00E+00	1.10E-07	2.17E-08	7.52E-07	7.03E-07
			Π Numbers			
Π_1 regional slope/internal friction		1.00E-01	2.00E-01	2.00E-01	2.00E-01	2.00E-01
Π_2 density ratio		1.04E+00	1.04E+00	1.04E+00	1.04E+00	1.04E+00
Π_3 ductile thickness/length ratio		8.30E-01	4.14E-01	3.23E-01	2.49E-01	2.49E+01
Π_4 brittle/ductile thickness ratio		7.26E-01	7.26E-01	9.31E-01	7.04E-01	6.30E-01
Π_5 cohesive/lithostatic ratio		3.61E-01	3.63E-01	3.63E-01	2.67E-01	2.99E-01
Π_6 inertial/viscous ratio		0.00E+00	1.76E-09	9.65E-10	7.46E-09	7.46E-09
Π_7 pressure/viscous ratio		-	4.40E+00	2.96E+00	1.71E+00	1.71E+00
Π_8 gravity/viscous ratio		-	1.06E+01	9.18E+00	6.87E+00	6.87E+00
Π_9 velocities ratio		-	1.00E+00	1.00E+00	1.00E+00	1.00E+00
Π_{10} process rate ratio		8.70E+00	6.82E-01	1.01E+00	1.75E+00	1.75E+00

Table 3c. Experimental Results for Experiment 4 Left, 5a, 5b, 5c, and 5d

Parameter	Units	Exp. 4 Left	Exp. 5a	Exp. 5b	Exp. 5c	Exp. 5d
A lower slope of silicon	deg	6	6	7	8	9
			Brittle Layer			
H_b	m	0.0075	0.0165	0.0165	0.0165	0.0165
ρ_b	kg m^{-3}	1.40E+03	1,40E+03	1.40E+03	1.40E+03	1.40E+03
c	Pa	1.00E+01	1.00E+01	1.00E+01	1.00E+01	1.00E+01
φ	deg	30	30	30	30	30
			Ductile Layer			
L_d	m	0.5350	0.5350	0.5350	0.5350	0.5350
H_d	m	0.0140	0.0110	0.0110	0.0110	0.0110
ρ_d	kg m^{-3}	1.35E+03	1.35E+03	1.35E+03	1.35E+03	1.35E+03
μ_d	Pa s	1.00E+04	1.00E+04	1.00E+04	1.00E+04	1.00E+04
			Result			
Deformation	bolean	TRUE	FALSE	FALSE	FALSE	TRUE
Structure Type		Three diapiric folds and one thrust at the front. Diapiric extension on back with two plates.	Deformation is limited to a 2 mm drop at the upper side of the box.	Deformation is limited to a 2 mm drop a the upper side of the box.	Deformation is limited to a 2 mm drop a the upper side of the box, a small graben forms.	One single thrust in front and a graben with an extended horst at the upper side of the box.
			Time			
Time to start of deformation	s	2.700E+03	-	-	-	3.0300E+04
Time to end of deformation	s	1.3560E+05	-	-	-	1.1940E+05
Time to end of experiment	s	1.6650E+05	5.7690E+05	8.1600E+04	1.7220E+05	1.7160E+05
			Structure			
L_t	m	0.096	0	0	0	0.062
ΔH_t	m	0.018	0	0	0	0.028
L_g	m	0.058	0.005	0.005	0.005	0.09
ΔH_g	m	0.075	0.0087	0.0087	0.0087	0.016
L_h	m	0.037	0	0	0.032	0
			Velocities			
V_x	m s^{-1}	3.95E-06	0.00E+00	0.00E+00	0.00E+00	4.48E-06
V_z	m s^{-1}	1.03E-07	0.00E+00	0.00E+00	0.00E+00	9.21E-08
V_x thrusting	m s^{-1}	7.08E-07	0.00E+00	0.00E+00	0.00E+00	5.19E-07
			Π *Numbers*			
Π_1 regional slope/internal friction		2.00E-01	2.00E-01	2.33E-01	2.67E-01	3.00E-01
Π_2 density ratio		1.04E+00	1.04E+00	1.04E+00	1.04E+00	1.04E+00
Π_3 ductile thickness/length ratio		2.49E-01	1.96E-01	1.67E-01	1.46E-01	1.30E+01
Π_4 brittle/ductile thickness ratio		5.56E-01	1.56E-01	1.56E-01	1.56E-01	1.56E-01
Π_5 cohesive/lithostatic ratio		3.39E-01	1.54E-01	1.54E-01	1.55E-01	1.55E-01
Π_6 inertial/viscous ratio		7.46E-09	0.00E+00	0.00E+00	0.00E+00	6.65E-09
Π_7 pressure/viscous ratio		1.71E+00	-	-	-	7.26E-01
Π_8 gravity/viscous ratio		6.87E+00	-	-	-	5.59E+00
Π_9 velocities ratio		1.00E+00	-	-	-	1.00E+00
Π_{10} process rate ratio		1.75E+00	8.50E-01	6.02E+00	2.86E+00	4.13E+00

Table 3d. Experimental Results for Experiments 6 Left, 6 Center, 6 Right, and Regular Structure

Parameter	Units	Exp. 6 Left	Exp. 6 Center	Exp. 6 Right	Regular Structure
A lower slope of silicon	deg	6	6	6	5.9
		Brittle Layer			
H_b	m	0.0075	0.055	0.0060	1500
ρ_b	kg m^{-3}	1.40E+03	1,40E+03	1.40E+03	2.50E+03
c	Pa	1.00E+01	1.00E+01	1.00E+01	1.00E+06
φ	deg	30	30	30	30
		Ductile Layer			
L_d	m	0.2400	0.2400	0.2400	52,000
H_d	m	0.0150	0.0150	0.0150	3800
ρ_d	kg m^{-3}	1.35E+03	1.35E+03	1.35E+03	2300
μ_d	Pa s	1.00E+04	1.00E+04	1.00E+04	1.00E+18
		Result			
Deformation	bolean	TRUE	TRUE	TRUE	TRUE
Structure Type		One diapiric fold.	Two diapiric folds.	One diapiric thrust obtained by erosion of fold.	1–3 diapiric thrusts, with erosion. 1–4 grabens on the back.
		Time			
Time to start of deformation	s	7.2000E+03	7.2000E+03	7.2000E+03	1.0000E+13
Time to end of deformation	s	8.4300E+04	8.4300E+04	8.4300E+04	1.0000E+13
Time to end of experiment	s	8.4300E+04	8.4300E+04	8.4300E+04	1.0000E+13
		Structure			
L_t	m	0.021	0.4	0.026	10,0000
ΔH_t	m	0.012	0.015	0.007	3000
L_g	m	0.007	0.022	0.022	700
ΔH_g	m	0.0075	0.0055	0.006	1000
L_b	m	0.022	0.023	0.023	3000
V_x	m s^{-1}	2.85E-06	2.85E-06	2.85E-06	5.20E-09
V_z	m s^{-1}	1.78E-07	1.78E-07	1.78E-07	3.80E-10
V_x thrusting	m s^{-1}	2.49E-07	4.74E-07	3.08E-07	1.00E-09
		Π *Numbers*			
Π_1 regional slope/internal friction		2.00E-01	2.00E-01	2.00E-01	1.97E-01
Π_2 density ratio		1.04E+00	1.04E+00	1.04E+00	1.09E+00
Π_3 ductile thickness/length ratio		5.95E-01	5.95E-01	5.95E-01	7.07E-01
Π_4 brittle/ductile thickness ratio		5.19E-01	3.80E-01	4.15E-01	4.29E-01
Π_5 cohesive/lithostatic ratio		3.39E-01	4.62E-01	4.23E-01	9.48E-02
Π_6 inertial/viscous ratio		5.77E-09	5.77E-09	5.77E-09	4.54E-20
Π_7 pressure/viscous ratio		6.50E+00	6.50E+00	6.50E+00	4.55E+00
Π_8 gravity/viscous ratio		1.09E+01	1.09E+01	1.09E+01	6.43E+00
Π_9 velocities ratio		1.00E+00	1.00E+00	1.00E+00	1.00E+00
Π_{10} process rate ratio		4.62E-01	4.62E-01	4.62E-01	6.59E-01

observe that our natural system has the following 14 variables with four dimensions: H_b (m), ρ_b (kg m^{-3}), ϕ (°), c (kg m^{-1} s^{-2}), L_d (m), H_d (m), ρ_d (kg m^{-3}), μ_d (kg m^{-1} s^{-1}), α (°), g (m s^{-2}), T (s), P_d (kg m^{-1} s^{-2}), V_x (m s^{-1}) and V_z (m s^{-1}). Therefore there are 10 dimensionless ratios (Π) that need to be equal to make scaled down experiment of our system. Considering the former lubrication approximation, from which we derive equation (20), we may define a set of dimensionless ratios (Π-numbers, equation (21)) which we list in Table 1.

[39] The experimental setup (Figure 9) is composed of a 0.54 × 0.29 m plexiglass box that has a rigid bottom (the basement). A thin, wide, and wedge-shaped layer of silicon (see Figure 8) is laid on the bottom forming the ductile layer. In turn, the silicon is covered by one or more layers of fine white sand (the brittle layer) that are covered by a veneer of black sand as marker. The values of parameters and Π-numbers for the natural system and the experiments are listed in Tables 2 and 3a–3d.

[40] During each experiment the box is tilted incrementing its slope in time steps. At each step, before increasing the inclination of the box to the next dip value, the experiment is left evolving for sufficient time (ranging from many hours to days) to verify whether deformation takes place or not. This procedure is repeated up to the slope at which deformation begins. At this slope the experiment is left for a sufficiently long time (ranging from one to many days) to ensure that it has reached a new static equilibrium. During the experiment we photograph the evolution and typology of deformation from the top in order to obtain the time at which deformation begins and terminates. When deformation is complete, the experiment is terminated by pouring a thick layer of blue sand on top of the model to avoid any further deformation even when the box is tilted back to horizontal. Finally, the sand is wetted and a set of sections are cut and photographed to quantify the type and amount of deformation (Figure 9b). In many experiments, because of small variations in thicknesses of the brittle and

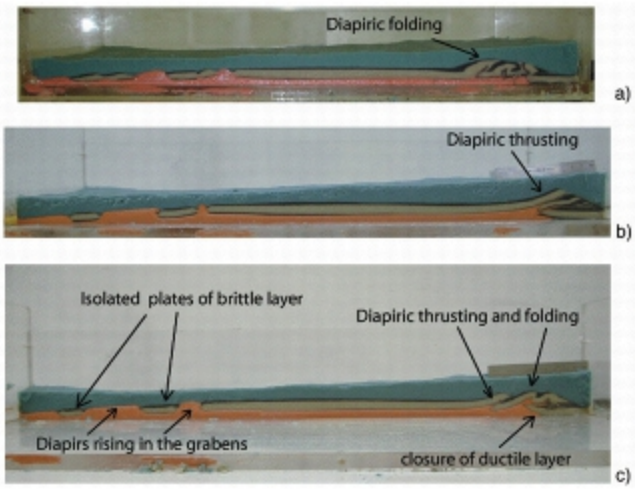

Figure 10. Cross-sections (slices) of the same experimental model (Experiment 4, Table 3) at the end of deformation (after tilting the model back to horizontal). Note the diapirs rising in the back grabens and the different stiles of deformation at the frontal diapiric structures. For small increases in the ratio $H_b\rho_b/H_d\rho_d$ the frontal structures changes from diapiric folding (a) to thrusting (b) through an intermediate behavior (c).

ductile layers within the same sand box, the type of deformation may vary from one side of the box to the other (Figure 10).

[41] In general, deformation begins with the formation of a graben at the upper edge of the model along the contact with the plexiglass box, as the silicon starts flowing downhill. In a relatively short time, a compressional ridge develops toward the lower edge of the model close to where the silicon terminates (Figure 9). As the deformation proceeds, the brittle layer moves downhill floating on the ductile layer which flows downhill underneath, uplifting the thrust front. Therefore at the front the brittle layer is folded into a broad syncline. At the back, instead, extension allows the silicon to rise forming a diapir, giving rise to a sand/silicon detachment structure. In the case in which the brittle layer is sufficiently thin and long, a set of "plates and diapirs" develops toward the rear of the brittle layer (Figure 10). The plates between the diapirs tend to form gentle synclines bounded by listric faults dipping away from their nuclei. These synclines are similar to those occurring in the many isolated sandstone plates, like the Scurano-Vetto gravity syncline [*Carena et al.*, 2000], found on the northeastern slope of the NAR.

[42] Although, to warrant similarity, all dimensionless ratios must be equal in nature and in the experimental setup, only some of them are really relevant for analyzing the experimental results. To choose among them, we make the following considerations. Π_1 is irrelevant because the regional slope (and the slope of the experimental box) remains always much smaller than the angle of internal friction of the brittle layer (the angle of repose of the sand), without ever reaching critical conditions. Also, Π_2 is not relevant because it never changes in our experiments. Regarding the ratios of forces and mass flow, they are either very small like Π_5 and the Reynolds number or must be equal to one (and therefore constant for all experiments) as a consequence of the scaling analysis, developed in obtaining equation (20), like Π_7, Π_8, and Π_9. Therefore only three dimensionless numbers appear to be significant in our experiments: Π_3, Π_4, and Π_{10}. We remark that this simplification can be done because we transfer the constraints obtained from the analytic into the analogue model. Therefore also the results of the analogue model are valid only for a thin ductile layer on a small slope.

[43] Accordingly, the dynamics of our system may be simply described by a set of three Cartesian axis; one for each of these Π numbers (Figure 11). Whereas Π_3 and Π_4 are almost constant during an experiment, Π_{10} decreases in time. Thus each experiment is represented in this 3-D space by an almost straight line that is parallel to Π_{10}.

[44] Within this space, a projection on the Π_3–Π_4 plane is independent of time (Figure 11a). Thus the three contiguous fields of stability, thrusting, and folding, identified by the experimental data, indicate the type of deformation reached at the end of each experiment. For any given length, thickness, and slope of the ductile layer, the decrease of the thickness of the brittle layer will first make the system unstable and then produce deformation with structures that range from diapiric thrusts to diapiric folds. The same sequence is obtained if one keeps the thicknesses of both layers constant and increases the length of the ductile layer or its slope. One other way to look at this result is that a thicker brittle layer will make an experiment stable, or favor thrusts relative to folds. On this projection our field structure falls in the field of diapiric thrusting.

[45] On the Π_4–Π_{10} projection (Figure 11b) there are no stability fields because Π_{10} decreases in time. We see that a single experiment may evolve from diapiric folding to diapiric thrusting. This means that the deformation tends, in any case, to begin with folding eventually evolving to thrusting. On this projection the structure of the NAR studied in the field falls in the area of folding. Since the former projection indicates that deformation should end with diapiric thrusting, we may suggest that the diapiric deformation is still active.

[46] Also, in the Π_3–Π_{10} projection (Figure 11c) there is no stability field. At the end of deformation (before the experiments are terminated) the experimental points align with Π_3 following an inverse power function of Π_{10}. Because the projection is made parallel to Π_4, this function is independent of Π_4. On this projection as well as in the former one, the NAR structure studied in this paper falls in the area to the right of the function, which indicates that deformation is not yet terminated.

[47] Least square interpolation of the experimental points to a power function gives:

$$\Pi_3 = 0.3566\Pi_{10}^{-0.647}, \tag{22}$$

which has a correlation coefficient $R^2 = 0.966$, and can be approximated by

$$\Pi_3 \approx 0.3566\Pi_{10}^{-2/3}. \tag{23}$$

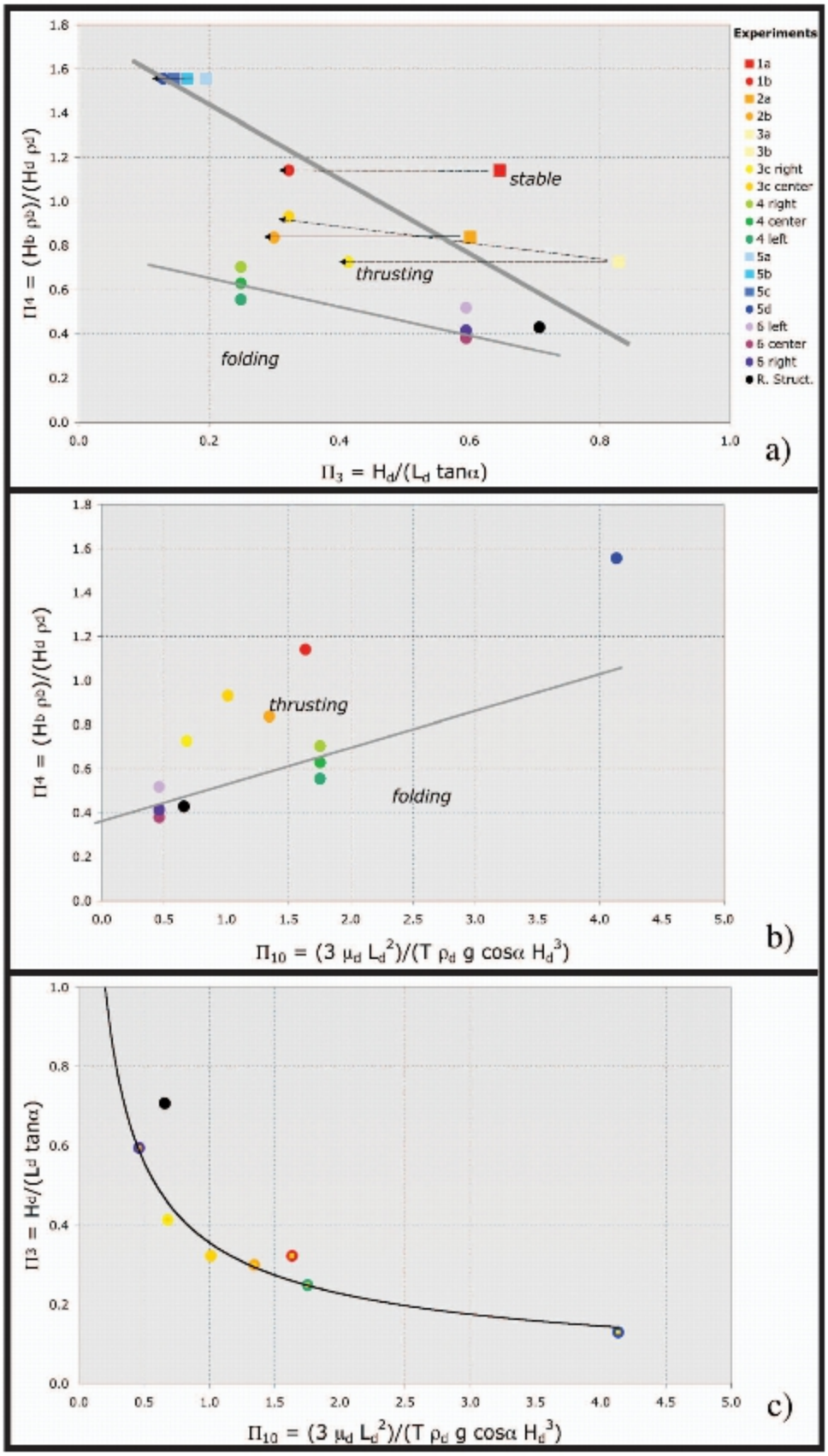

Figure 11. Projection of the experimental data onto the three axial planes defined by (a) Π_4 versus Π_3, (b) Π_4 versus Π_{10}, and (c) Π_3 versus Π_{10}. See text for explanation.

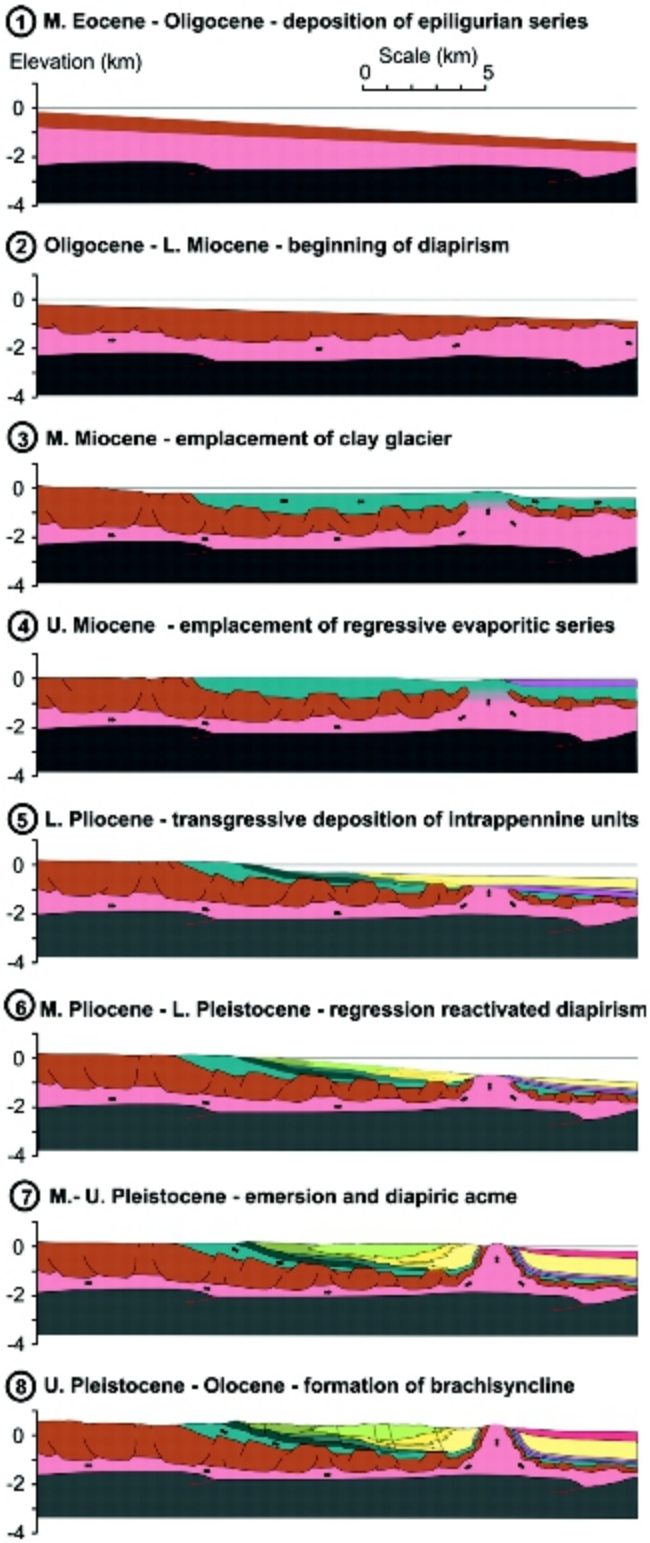

Figure 12. SW-NE time-sequence sketches of the geological evolution of the northeastern slope of the NAR in the study area. See text for explanation. Color legend in Figures 1a–1d.

From equation (23) it is possible to infer the time still needed to reach the end of deformation in the studied structure. Substituting in this equation the value of II_3 (see Tables 3a–3d), we obtain a final value II_{10} of about 0.36. Given that today's value of II_{10} is 0.66, we deduce that our field structure has overcome the first half of the deformation not long ago. Therefore in the hypothesis that the tectonic conditions will remain the same, about 10^5 more years are needed before the rate of deformation will become negligible.

[48] Also the diapiric uplift of the regional structure may be estimated from equation (21i) using the experimental values (Tables 3a–3d):

$$V_z = \frac{H_d}{L_d} V_x = \frac{H_d}{T} = 3.8 * 10^{-10}\ \mathrm{m/s} \sim 1.2 * 10^{-2}\ \mathrm{m/a}, \quad (24)$$

This is a significant vertical velocity and is consistent with the fact that all major drainages are in active erosion only where they cross the chaotic clays diapers and are in adepositional phase elsewhere (Figures 1a–1d). This rapid uplift may also explain the apparent morphologic contradiction seen along the northern ridge where all the highest elevations are composed of easily erodible chaotic clays with roots up to 3 km deep. If we make the hypothesis that the topography of the ridges is in steady state equilibrium, being feed by the diapiric rise from below and being eroded by landsliding from the top, considering an average width of the diapir of 3×10^3 m, we estimate that there are 30 m^3 of clay per meter of diapir length (parallel to the range) available for landsliding each year or more than a 1 $km^3\ a^{-1}$ only for the section of diapir in our study area. On the other hand, if the ridge top is uplifting, only a fraction of this material is available each year for landsliding. In a longer term, though, we argue that the balance between diapiric feeding and landslide erosion should be maintained.

7. Neogene Evolution

[49] On the basis of the published data and our detailed field study we attempt a reconstruction, from Eocene to the present day, of the tectonic evolution of the piggyback basin successions, which are found on the northeastern slope of the NAR. Our tectonic reconstruction shows how diapiric tectonics deeply modifies and overprints regional tectonic structures. Indeed, through compression and shortening, regional tectonics creates the necessary initial topographic gradient that triggered the diapiric tectonics. Our model is similar to forelandward fold propagation [*Bonini*, 2001], with gravity playing a fundamental role, a role that was previously neglected in studies of this area, except for the intuitions of Bombicci in 1882. In our model we identify the following eight phases of evolution:

[50] 1. During the first phase, the Epiligurid units are deposited (Figure 12a) and begin to form a brittle layer on top of the ductile clayey Ligurid units. These units begin to be tilted to the northeast because of differential uplift along the front of the Apennine chain induced by regional compression [*Cibin et al.*, 2001; *Cibin et al.*, 2003].

[51] 2. During the second phase (Figure 12b), between the Oligocene and the Lower Miocene, diapiric tectonics begins leading to downhill flow of the Ligurid units and contemporaneous sinking of the Epiligurid sandstones into the Ligurids. The brittle Epiligurid units break up in variably tilted blocks, while downhill the Ligurids thicken, uplifting the Epiligurid units and perching them as a diapir.

As a consequence of ductile shear flow during millions of years over many kilometers, some Ligurid units will loose their "olistostrome" sedimentary structures becoming "tectonosomes" [*Pini*, 1999].

[52] 3. The third phase (Figure 12c) occurs during the Middle-Upper Miocene. The formation and uplift of the diapir leads to erosion, which is associated with flow and resedimentation of the chaotic clays also in the form of "clay glaciers," similar to the salt glaciers of the Gulf of Mexico [*Diesel et al.*, 1995; *Fletcher et al.*, 1995].

[53] 4. The fourth phase (Figure 12d) occurs during the Messinian regression that in the Mediterranean area, is characterized by the deposition of evaporitic rock sequences. In the study area, these sequences are found only northward of the main diapiric ridge, indicating that southward of the ridge the area was emerged.

[54] 5. The fifth phase (Figure 12e) begins in the Lower Pliocene with a new transgression, during which the Intra-Apennine terrigenous marine rock units begin to be deposited. These units have complex time-equivalent geometric relationships with each other.

[55] 6. The sixth phase (Figure 12f) starting in the Middle Pliocene and ending in the Lower Pleistocene terminates the depositional cycle of the Intra-Apennine units with a regression. Both deposition and regression reactivate new diapiric tectonics, which become dominant also in the ductile rock units found at stratigraphic levels higher than the Ligurid units (such as, for instance, in the clay glacier). Consequently, the tectonic deformation becomes more complex, occurring at various stratigraphic levels.

[56] 7. The seventh, Middle-Upper Pleistocene phase, is characterized by emersion from the sea (subaerial exposure) [*Vai and Castellarin*, 1992]. Because of the combined effect of density gradients and subaerial erosion, diapirism reaches the highest intensity. All rock units above the Ligurids are involved in deformation during this phase. Erosion of the Intra-Apennine terrigenous units leads to deposition of the Imola sandstones north of the main diapir (the northern ridge).

[57] 8. The eighth and the last phase (Figure 12h), from Middle Pleistocene to Holocene, is characterized by the formation of the most recent tectonic structures, such as the faulted Zena syncline and the small diapir structure of "Scanno" ridge. The diapirs actively dam the rivers Idice, Zena, and Savena allowing the formation of river terraces and meanders uphill of them. Deep-seated gravity deformation occurs during this time in the Intra-Apennine sandstone cliffs, due to the presence of clayey layers at their bottom (Figure 3e). According to the experimental results, this phase of deformation is not yet concluded: it now shows diapiric folding, while the deformation should terminate with diapiric thrusting.

[58] On comparing the cross section of the study area (Figure 12h) and the experimental results (Figures 9 and 10), there are some obvious differences in the details of the deformation pattern. We remark that our experiments can give only order-of-magnitude qualitative results because the model does not fully reflect the heterogeneity and complexity of the natural structure and of its evolution. In fact, in drawing the cross sections of Figure 12 we take into account the deformation that occurred during sedimentation of the Epiligurid units and the Messinian and Pleistocene erosional events, all of which are not modeled in our experiments. Also the second ductile layer (TER), which is located at a higher stratigraphic level and is not modeled in our experiments, had an important role in reducing the wavelength and faulting of the Zena syncline. Finally, the deformation of the natural structure is not yet completed, while it is completed in the experiments.

8. Conclusions

[59] 1. Taking into account morphologic, stratigraphic, and tectonic data, we reconstruct the marine sedimentation/abrasion surface, which records the emergence from the sea of the Intra-Apennine formations at the end of the Lower Pleistocene. Subsequently, this surface was folded into a brachisyncline associated to listric faulting and horst-and-graben structures (Figure 7). The reconstruction of fault displacements allows us to calculate the thickness of the Intra-Apennine sedimentation rock cycle to be approximately 1/3 of what was previously thought (that is about 200–300 m instead of 1 km).

[60] 2. Just southward (uphill) of the northern margin of the Apennine Range, a long (a few tens of kilometers) and narrow (a few kilometers) diapir occurs. The diapir began its activity with the deposition of the Epiligurid units from Eocene up to present day (Figure 1a). The diapir consists of Ligurid (and subordinate Epi-Ligurid) chaotic shaley units that reach a maximum thickness of 3.5 km [*RER*, 1998]. The diapir extends laterally around the brachisyncline along the Sillaro Valley and forms a number of minor diapirs like the one at "Scanno" ridge in the Zena Valley (Figures 1b, 3a, and 3c). The rock units that surround the diapirs are variably tilted, in a few cases overturned, stretched, and disjointed. In quite a few cases they have been directly involved in the diapiric deformation. The diapir has a rate of uplift of approximately 1 cm/a and, even if made of erodible rocks, actively dams the main rivers.

[61] 3. Two other clayey units may form ductile layers within the Epiliguid units: the clay glacier, formed during the Middle-Upper Miocene (TER), and the Pliocene-Pleistocene Marls of Riolo Terme. Both of these layers are ductile and play a determinant role in the development of thin-skinned gravitational tectonics in the sandy brittle units overlaying them (Figures 1b, 1e, 3b, 3c, and 3d).

[62] 4. Using an analytical approximation of the Navier-Stokes equations and analogue scaled experiments, we have shown that thrusting of the Epiligurid units may be generated by diapiric tectonics and not only by regional compression. Because of a gravity component parallel to the strata, the final structures formed by diapirism are substantially similar to those generated by compressive regional tectonics. They differ, however, in the fact that thrusting is always accompanied and lubricated by diapiric rise. Our experiments identify the fields of stability, folding, and thrusting (Figure 11a). Furthermore, they show that deformation always begins with folding, eventually evolving to thrusting (Figure 11b). Finally, we derive an empirical relation that calculates the time needed to reach the end of deformation (Figure 11c). These results indicate that the diapiric deformation in the study area is still in the folding regime, but it should eventually evolve to the thrusting regime and terminate in about 10^5 a.

[63] 5. The whole northeastern slope of the NAR appears to be controlled by diapiric tectonics (Figure 1a). As a matter of fact, the clayey Ligurid units form a continuous ductile layer below the sandy and calcareous Epiligurid units, which once formed an almost continuous brittle layer (Figure 1c). Since the time of sedimentation of the Epiligurid units (but particularly after regional compression, differential uplift, and emergence) the clayey ductile units began to deform under the regional topographic gradient and the differential load of the sandy brittle units. This gravitational tectonics induced the formation of a long and narrow diapir just uphill of the northeastern margin of the NAR. In turn, south of the diapir, the Epiligurid became folded into brachisynclines separated by rising clayey diapirs composed of Ligurid units. The extention and diapirism occurring at the southern margin of the epiligurid units give rise to a detachment (Figure 1a). It appears that diapiric tectonics is so intense and widespread to overwhelm and erase, in many cases, the regional tectonic imprint in the deformed Ligurid and Epiligurid units. This interpretation of the Neogene evolution of the NAR differs from the traditional interpretation, which considers compressive regional tectonics as the only controlling factor of the tectonic evolution of the Ligurid and Epiligurid units [cf. *Boccaletti and Coli*, 1982]. It also differs from a more recent interpretation in which the Apennine superficial layers gravitationally slide northward on a decollement identified by seismic reflection data [*Argnani et al.*, 2003] because in our model there is a thick ductile layer that flows downhill on a "rigid" basement instead of a simple decollement.

[64] 6. Our model is developed for the northern slope of the NAR taking into consideration a highly detailed geological survey, which was mostly already available (*RER* [1997, 1998, 2001] and this work). Our interpretations and conclusions have been founded on mass and momentum conservation equations, which are of general applicability. Therefore we are confident that our model could be applied to other areas where ductile units have undergone even minor differential uplift.

[65] **Acknowledgments.** We acknowledge the careful reviews of Massimiliano Zattin, Lykke Gemmer, and Jean Braun, which have substantially improved our manuscript. This work is financed by Regione Emilia-Romagna and EDRA. Analogue experiments were supported by the Laboratoire Magmas et Volcans (UMR 6524) at the Université Blaise Pascal, Clermont-Ferrand, France, through a Visiting Professor Fellowship to A. Borgia. We thank Nicoletta Ricciuto for assistance during fieldwork.

References

Abbate, E., V. Bortolotti, and M. Sagri (1981), An approach to olistostromes interpretation, paper presented at 2nd European Regional Meeting, Int. Assoc. of Sedimentol., Bologna, Italy.

Argnani, A., G. Barbacini, M. Bernini, F. Camurri, M. Ghielmi, G. Papani, F. Rizzino, S. Rogledi, and L. Torelli (2003), Gravity tectonics driver by quaternary uplift in the northern Appennines: Insight from the La Spezia–Reggio Emilia geo-transect, *Quat. Int.*, *101–102*, 13–26.

Bertocci, R., and N. Casagli (1992), Fenomeni di espansione laterale in alcune aree dell'Appennino tosco-romagnolo: Aspetti geomorfologici e proprietà geotecniche dei materiali argillosi coinvolti, *Atti Tic. Sc. Terra*, *35*, 31–42.

Bettelli, G., and F. Panini (1984), Il Melange sedimentario della Val Tiepido (Appennino modenese): Composizione litologica, distribuzione areale e posizione stratigrafica, *Atti Soc. Natl. Mat. Modena*, *115*, 77–90.

Bettelli, G., and F. Panini (1987), I melanges dell'Appennino settentrionale dal t. Trasinaro al t. Sillaro, *Mem. Soc. Geol. It.*, *39*, 187–214.

Bird, R. B., W. E. Stewart, and E. N. Lightfoot (1960), *Transport Phenomena*, 780 pp., John Wiley, Hoboken, N. J.

Boccaletti, M., and M. Coli (Eds.) (1982), Carta strutturale dell'Appennino Settentrionale. CNR, Prog. Fin. Geodin. S.P.5, pubbl. 429. S.EL.CA, Firenze.

Boccaletti, M., F. Calamita, G. Deiana, R. Gelati, F. Massari, G. Moratti, and F. Ricci Lucchi (1990a), Migrating foredeep-thrust belt system in the Northern Apennines and Southern Alps, *Palaeo.*, *77*, 3–14.

Boccaletti, M., et al. (1990b), Palinspastic restoration and paleogeographic reconstruction of the peri-Tyrrhenian area during the Neogene, *Palaeo.*, *77*, 41–50.

Bombicci, L. (1882), Il sollevamento dell'Appennino bolognese per diretta azione della gravità e delle pressioni laterali, con appendice sulle origini e sui reiterati trabocchi delle argille scagliose, *Memo. Accad. Sci. Ist. Bologna*, *IV*(III), 639–661.

Bonini, M. (2001), Passive roof thrusting and forelandward fold propagation in scaled brittle-ductile physical models of thrust wedges, *J. Geophys. Res.*, *106*(B2), 2291–2311.

Borgia, A., S. Carena, A. Battaglia, G. Pasquaré, M. Ferraris, L. Martelli, and M. T. De Nardo (1997), Genesis of isolated synclines: Is gravitational stress sufficient to create them?, *Quaternario*, *10*(2), 529–534.

Carena, S., A. Borgia, G. Pasquarè, A. Battaglia, M. Ferrarsi, L. Martelli, and M. T. De Nardo (2000), Gravity synclines, *J. Geophys. Res.*, *105*(B9), 21,819–21,833.

Castellarin, A., and G. B. Vai (1986), Southalpine versus Po Plain Apenninic arcs, in *The Origin of Arcs*, edited by C. Wezel, *Dev. Geotectonics*, *21*, 253–280.

Castellarin, A., C. Eva, G. Giglia, and G. B. Vai (1986), Analisi strutturale del fronte appenninico padano, *Giornale Geol.*, *47*, 47–75.

Cazzoli, M. A., P. Tabarroni, and A. Zanna (1988), Assetto tettonico della zona pedemontana tra Bazzano e Zola Predosa – Appennino Bolognese, *Rend. Soc. Geol. It.*, *11*, 321–324.

Cibin, U., E. Spadafora, G. G. Zuffa, and A. Castellarin (2001), Continental collision history from arenites of episutural basins in the Northern Apennines, Italy, *Geol. Soc. Am. Bull.*, *113*, 4–19.

Cibin, U., A. Di Giulio, and L. Martelli (2003), Oligocene–Early Miocene tectonic evolution of the Northern Apennines (north-western Italy) traced through provenance of piggy-back basin fill successions, in *Tracing Tectonic Deformation Using the Sedimentary Record*, edited by T. McCann and A. Saintot, *Geol. Soc. Spec. Publ.*, *208*, 269–287.

Di Dio, G., S. Lasagna, D. Preti, and M. Sagne (1997a), Carta Geologica dei depositi quaternari della provincia di Parma, *Quaternario*, *10*(2), 443–450.

Di Dio, G., S. Lasagna, D. Preti, and M. Sagne (1997b), Stratigrafia dei depositi quaternari della Provincia di Parma, *Boll. Soc. Paleont. It.*, *36*(1–2), 179–187.

Diesel, F. A., D. C. Schuster, J. F. Karlo, R. C. Shoup, and P. R. Tauvers (1995), Cenozoic structural evolution and tectono-stratigraphic framework of the northern Gulf coast continental margin, in *Salts Tectonics: A Global Perspective*, edited by M. P. A. Jackson et al., *AAPG Mem.*, *65*, 109–151.

Farabegoli, E., A. Benini, M. T. De Nardo, D. Preti, and P. Severi (2006), Carta geologica d'Italia alla scala 1:50.000, Foglio n. 238 Castel S. Pietro Terme. APAT, Difesa del Suolo – Regione Emilia-Romagna, Servizio geologico, sismico e dei suoli, in press.

Fletcher, R. C., M. R. Hudec, and I. A. Watson (1995), Salt glacier and composite sediment-salt glacier models for the emplacement and early burial of allochtonous salt sheets, in *Salt Tectonics: A Global Perspective*, edited by M. P. A. Jackson, D. G. Roberts, S. Snelson, *AAPG Mem.*, *65*, 77–108.

Lipparini, T. (1966), Note illustrative della carta geologica d'Italia alla scala 1:100.000, foglio 87 Bologna, Serv. Geol. d'Italia, Roma.

Merle, O., N. Vidal, and B. van Wyk de Vries (2001), Experiments on vertical basement fault reactivation below volcanoes, *J. Geophys. Res.*, *106*(B2), 2153–2162.

Ogniben, L. (1953), "Argille scagliose" e "Argille brecciate" in Sicilia, *Boll. Serv. Geol. Ital.*, *75*, 281–289.

Ori, G. G., and P. F. Friend (1984), Sedimentary basins formed and carried piggy-back on active thrust sheets, *Geology*, *12*, 475–478.

Panini, F., G. Bettelli, and M. Pizziolo (2002), Carta Geologica d'Italia 1:50.000, Foglio n. 237 Sasso Marconi. Servizio Geologico d'Italia – Regione Emilia-Romagna. S.EL.CA., Firenze.

Papani, G. (1964), Su un olistostroma di "argille scagliose" intercalato nella serie oligomiocenica del subappennino reggiano, *Boll. Soc. Geol. It.*, *82*, 195–202.

Parea, G. C. (1987), Paleogeografia e tettonica tardo-pleistoceniche del pedeappennino modenese, *Boll. Soc. Geol. It.*, *39*, 433–446.

Philipponat, G., and B. Hubert (1997), *Fundations et Ouvrages en Terre*, 548 pp., Eyrolles, Paris.

Picotti, V., G. Bertotti, R. Capozzi, and A. M. Fesce (1997), Evoluzione tettonica quaternaria della Pianura Padana centro-orientale e dei suoi margini, *Quaternario*, *10*(2), 513–520.

Pieri, M. (1961), Nota introduttiva al rilevamento del versante appenninico padano eseguito nel 1955–59 dai geologi dell'AGIP Mineraria, *Boll. Soc. Geol. It.*, *80*, 3–34.

Pini, A. (1999), Tectonosomes and olistostromes i the Argille Scagliose of the northern Appennines, *Italy, Geol. Soc. Am. Spec. Pap.*, *335*, 70 pp.

Regione Emilia Romanga (RER) (1997), Carta Geologica dell'Appennino Emiliano-Romagnolo 1:10.000 sezz. 238010 and 238050. Regione Emilia-Romagna, Servizio Cartografico e Geologico. Archivio cartografico della regione Emilia-Romagna, Bologna.

RER (1998), Riserve idriche sotterranee della Regione Emilia-Romagna. A cura di G. Di Dio. Regione Emilia-Romagna, ufficio geologico – ENI Agip, Divisione Esplorazione e Produzione. S.EL.CA, Firenze, 120 pp.

RER (2001), Itinerari geologico-ambientali nelle colline bolognesi. Regione Emilia-Romagna, ufficio geologico. EFTB, Parma-S.EL.CA., Firenze.

Ricci Lucchi, F. (1987), Semi-allochthonous sedimentation in the Apenninic thrust belt, *Sedimentology*, *50*, 119–134.

Treves, B. (1984), Orogenic belts as accretionary prisms: The example of the Northern Apennines, *Ofioliti*, *9*(3), 577–618.

Vai, G. B., and A. Castellarin (1992), Correlazione sinottica delle unità stratigrafiche nell'Appennino settentrionale, *CROP*, *1-1A*, 171–185.

M. Badalì, A. Borgia, and F. Brondi, EDRA, via di Fioranello 31, 00134 Roma, Italia. (marcello_badali@yahoo.it; andrea@borgia.net; fabio.bro@tiscali.it)

T. di Nardo and L. Martelli, Servizio Geologico, Sismico e dei Suoli, Regione Emilia-Romagna, viale Silvani 4/3, 40122 Bologna, Italia. (mdenardo@regione.emilia-romagna.it; lmartelli@regione.emilia-romagna.it)

G. Grieco and G. Pasquarè, Dip. Scienze della Terra "A. Desio", Univ. degli Studi di Milano, via Botticelli 23, 20133 Milano, Italia. (giovanni.grieco@unimi.it; pasquale@unimi.it)

O. Merle, Laboratoire Magmas et Volcans, Observatoire de Physique du Globe, 5 rue Kessler, 63038 Clermont-Ferrand, France. (merle@opgc.univ-bpclermont.fr)